Circulation

ORIGINAL RESEARCH ARTICLE

Fast Degradation of MecciRNAs by SUPV3L1/ELAC2 Provides a Novel Opportunity to Tackle Heart Failure With Exogenous MecciRNA

Xu Liu, PhD*; Qinwei Wang, BS*; Xinya Li, MD; Yan Yang, BS; Yuqi Deng, BS; Xiaolin Wang, PhD; Peipei Wang, MM; Liang Chen, PhD; Likun Ma, MD; Ge Shan, PhD

BACKGROUND: Circular RNAs derived from both nuclear and mitochondrial genomes are identified in animal cells. Mitochondria-encoded circular RNAs (mecciRNAs) are attracting more attention, and several members of mecciRNAs have already been recognized in regulating mitochondrial functions. Mitochondria dysfunctions are well-known to participate in heart failure (HF). This study was designed to investigate the RNA metabolism of mecciRNAs and the relevant roles and potential application of mecciRNAs in HF.

METHODS: Compared with highly stable nuclear genome-encoded circular RNAs, the fast degradation feature of mecciRNAs is identified by RNA sequencing and a series of molecular, biochemical, and cellular experiments. The substantial protective effects of in vitro synthesized mecciRNAs were tested in both doxorubicin- and pressure overload–induced mouse models of HF.

RESULTS: We discover that mecciRNAs are promptly degraded by an animal-conserved complex of helicase SUPV3L1 (suppressor of var1, 3-like protein 1) and endoribonuclease ELAC2 (elaC ribonuclease Z 2). MecciRNA degradation complex and mecciRNAs interact with mitochondrial permeability transition pore and its regulators including TRAP1 (TNF receptor–associated protein 1) and CypD (cyclophilin D). MecciRNAs regulate mitochondrial levels of TRAP1 and CypD to modulate the opening of mitochondrial permeability transition pore and the release of mitochondrial reactive oxygen species. Exogenously applied mecciRNAs interact with cytosolic TRAP1 and increase mitochondrial levels of TRAP1, and lead to a more closed state of mitochondrial permeability transition pore to constrain deleterious reactive oxygen species release. HF conditions lead to stimulated mecciRNA degradation, and administration of in vitro synthesized mecciRNAs exhibits substantial protective effects in both doxorubicin- and pressure overload–induced mouse models of HF.

CONCLUSIONS: This study demonstrates the fast degradation of mecciRNAs and the associated regulations of mitochondrial reactive oxygen species release of mitochondrial permeability transition pore by mecciRNAs. HF conditions lead to dysregulated mecciRNA degradation, and exogenous mecciRNAs demonstrate treatment potential in mouse models of HF.

Key Words: circRNA ■ heart failure ■ mecciRNA ■ mitochondria ■ mitochondrial permeability transition pore ■ RNA therapy

Heart failure (HF), a complicated clinical syndrome, is caused by genetic factors and nongenetic conditions such as heart attack, high blood pressure, and heart muscle dysfunction.[1] Dilated cardiomyopathy is the most common type of cardiomyopathy,[2] and >50% of patients with dilated cardiomyopathy present with HF symptoms.[3] Some drugs (eg, the anthracycline doxorubicin [DOX]) can also cause or exacerbate HF.[4] Regardless of the understanding of its pathogenesis, current drug therapies for HF primarily aim to manage symptoms,

Correspondence to: Ge Shan, PhD, University of Science and Technology of China, No. 96, JinZhai Road Baohe District, Hefei, Anhui, 230026, PR China. Email shange@ustc.edu.cn
*X. Liu and Q. Wang contributed equally.
Supplemental Material is available at https://www.ahajournals.org/doi/suppl/10.1161/CIRCULATIONAHA.124.070840.
For Sources of Funding and Disclosures, see page XXX.

Circulation is available at www.ahajournals.org/journal/circ

Clinical Perspective

What Is New?

- Mitochondria-encoded circular RNAs (mecciRNAs) are subjected to fast degradation by a complex composed of SUPV3L1 (suppressor of var1, 3-like protein 1) and ELAC2 (elaC ribonuclease Z 2).
- A subset of mecciRNAs interacts with components and regulators of mitochondrial permeability transition pore including ATP5B and TRAP1 (TNF receptor–associated protein 1).
- MecciND2 as a TRAP1 interacting mecciRNA can inhibit mitochondrial permeability transition pore opening and mitochondrial reactive oxygen species release to protect cells from deleterious stresses.

What Are the Clinical Implications?

- Degradation of mecciRNAs is elevated and levels of mecciRNAs are decreased in cells and the heart under heart failure stresses.
- Administration of exogenous mus_mecciNd2 has protective effects on the heart in mouse models of heart failure.

Nonstandard Abbreviations and Acronyms

5-EU	5-ethynyl uridine
ActD	actinomycin D
circ-ctrl	control circular RNA
circRNA	circular RNA
co-IP	coimmunoprecipitation
CypD	cyclophilin D
DOX	doxorubicin
EF	ejection fraction
ELAC2	elaC ribonuclease Z 2
EtBr	ethidium bromide
FS	fractional shortening
HF	heart failure
LV	left ventricle
mecciRNA	mitochondria-encoded circular RNA
mPTP	mitochondrial permeability transition pore
mtROS	mitochondrial reactive oxygen species
ng-circRNA	nuclear genome–encoded circular RNA
RIP-seq	RNA immunoprecipitation followed by RNA sequencing
ROS	reactive oxygen species
smFISH	single-molecule fluorescence in situ hybridization
SUPV3L1	suppressor of var1, 3-like protein 1
TAC	transverse aortic constriction
TNF	tumor necrosis factor
TRAP1	TNF receptor–associated protein 1

and treatments that recover cardiac functions remain in demand.

Mitochondria are the major source of intracellular reactive oxygen species (ROS),[5] and the mitochondrial permeability transition pore (mPTP) is responsible for mitochondrial ROS (mtROS) release. mPTP is a nonspecific pore that opens in response to increased ROS or calcium levels upon mitochondrial dysfunction.[6] In HF, the mechano-energetic coupling of the heart is abnormal, and mitochondrial bioenergetic dysfunction leads to the overproduction of ROS, which drives the progression of cardiac defects.[5,7]

Circular RNAs (circRNAs) derived from both nuclear and mitochondrial genomes have been identified in animal cells.[8–10] CircRNAs encoded by the nuclear genome are considered highly stable and have been subjected to extensive studies.[11,12] Mitochondria-encoded circRNAs (mecciRNAs) have been discovered more recently, and several mecciRNAs have been recognized to regulate mitochondrial functions.[9,13–15] MecciND1, mecciND5, and mcPGK1 facilitate the mitochondrial import of nuclear-encoded proteins through the TOM complex.[9,15] The mecciRNA SCAR identified in liver cells binds to ATP5B and regulates the mtROS output of the mPTP to suppress nonalcoholic steatohepatitis.[14] So far little is known about the biogenesis and degradation of mecciRNAs.

In mammalian cells, it is generally believed that the mitochondrial genome generates polycistronic transcripts that are separated by short stretches of tRNA genes, which act as punctuation marks.[16] The RNase P complex and ELAC2 (elaC ribonuclease Z 2), which has RNase Z activity, cleave the 5' and 3' ends of these tRNAs to release the mature mRNAs.[16] Mutations in ELAC2 have been reported as causal defects in patients with infantile hypertrophic cardiomyopathy.[17] The human ortholog of the yeast ATP-dependent helicase SUV3, SUPV3L1 (suppressor of var1, 3-like protein 1), is another conserved key factor of RNA metabolism known to regulate the stability of mature mitochondrial mRNAs and the processing of linear intermediates.[18–20]

In this study, we investigated the mechanism of mecciRNA degradation, its functional role in HF, and the potential therapeutic value of mecciRNAs. We discovered that mecciRNAs were subjected to fast degradation by the SUPV3L1/ELAC2 complex. SUPV3L1/ELAC2 and mecciRNAs interacted with components and regulators of the mPTP to regulate mtROS release. Levels of mecciRNAs were lower, and the protein levels of SUPV3L1 and ELAC2 were elevated in HF mice. Administration

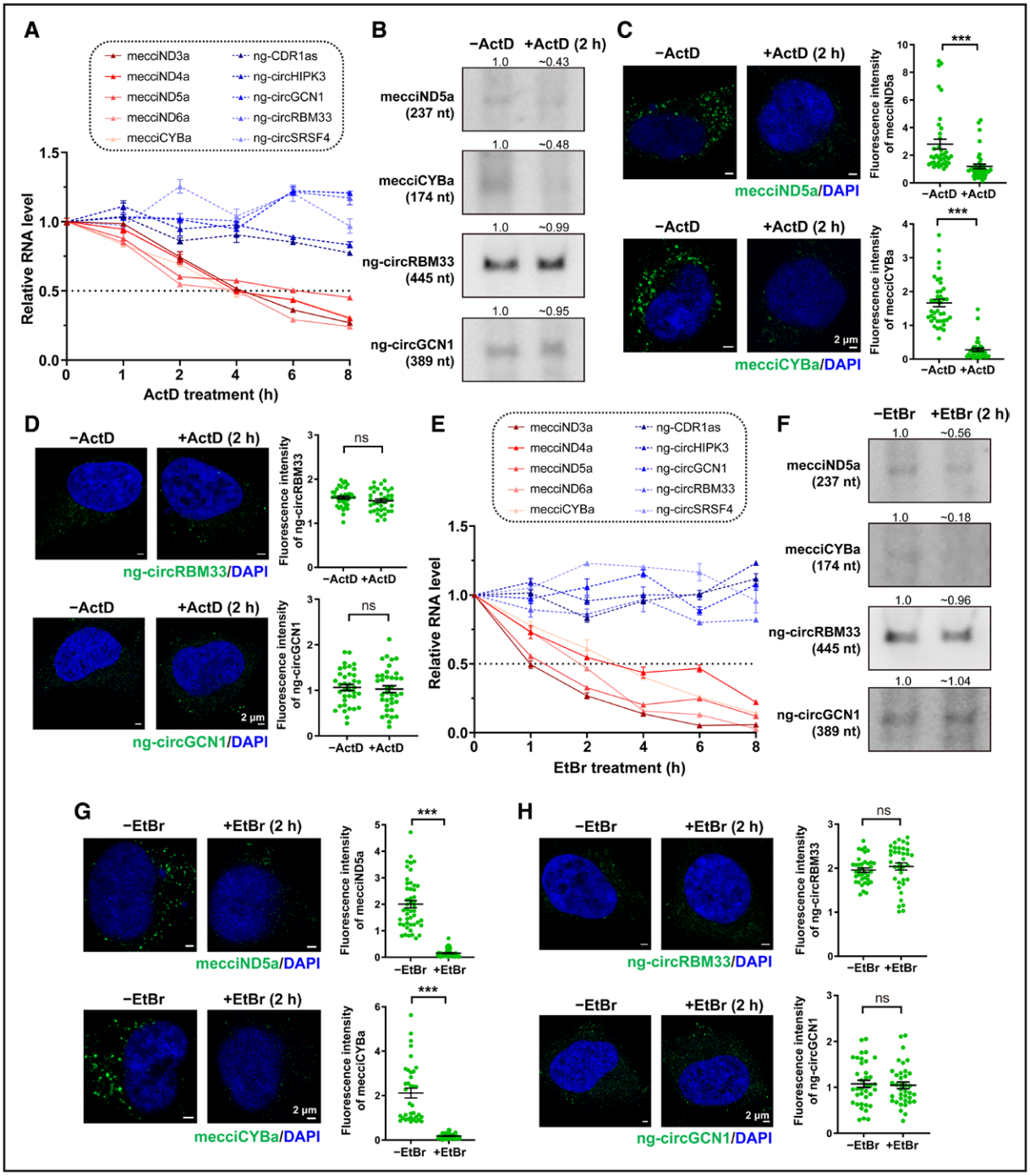

Figure 1. MecciRNAs are fast degraded compared with ng-circRNAs.

A, Quantitative reverse transcription polymerase chain reaction (RT-qPCR) of individual mecciRNAs and ng-circRNAs. RNA samples were from 293T cells treated with ActD for the indicated period (n=3 for each time point). **B**, Northern blots of mecciND5a, mecciCYBa, ng-circRBM33, and ng-circGCN1 in 293T cells treated with ActD (+ActD) or DMSO control (—ActD) for 2 h. Relative intensity of Northern blotting bands is labeled. **C**, Representative single-molecule fluorescence in situ hybridization (smFISH) images of mecciND5a and mecciCYBa in 293T cells treated with ActD (+ActD) or DMSO control (—ActD) for 2 h. smFISH signals are shown as scatter plots (n=38 cells [for mecciND5a smFISH], 39 [for mecciCYBa and —ActD], and 35 [for mecciCYBa and +ActD]). **D**, Representative smFISH images of ng-circRBM33 and ng-circGCN1 in 293T cells treated with or without ActD for 2 h. ng-circRNA smFISH signals were quantified (n=37 cells per group). **E**, RT-qPCR analysis of mecciRNAs and ng-circRNAs in 293T cells treated with ethidium bromide (EtBr) for the indicated period (n=3 for each time point). **F**, Northern blots of mecciND5a, mecciCYBa, ng-circRBM33, and ng-circGCN1L1 in 293T cells with (+EtBr) or without (—EtBr) EtBr treatment for 2 h. Relative intensity of Northern blotting bands is labeled. **G**, Representative smFISH images of mecciND5a and mecciCYBa in 293T cells with (+EtBr) or without (—EtBr) EtBr treatment for 2 h. smFISH signals are shown as scatter plots (n=47 cells [for mecciND5a smFISH], 36 [for mecciCYBa and −EtBr], and 38 [for mecciCYBa and +EtBr]). **H**, Representative smFISH images of ng-circRBM33 and ng-circGCN1 in 293T cells treated with or without EtBr for 2 h. ng-circRNA smFISH signals were quantified (n=37 cells per group). In **A**, **C**, **D**, **E**, **G**, and **H**, data are shown as mean±SEM, and *P* values were from 2-tailed unpaired Student *t* test. ns, not significant; ***$P<0.001$.

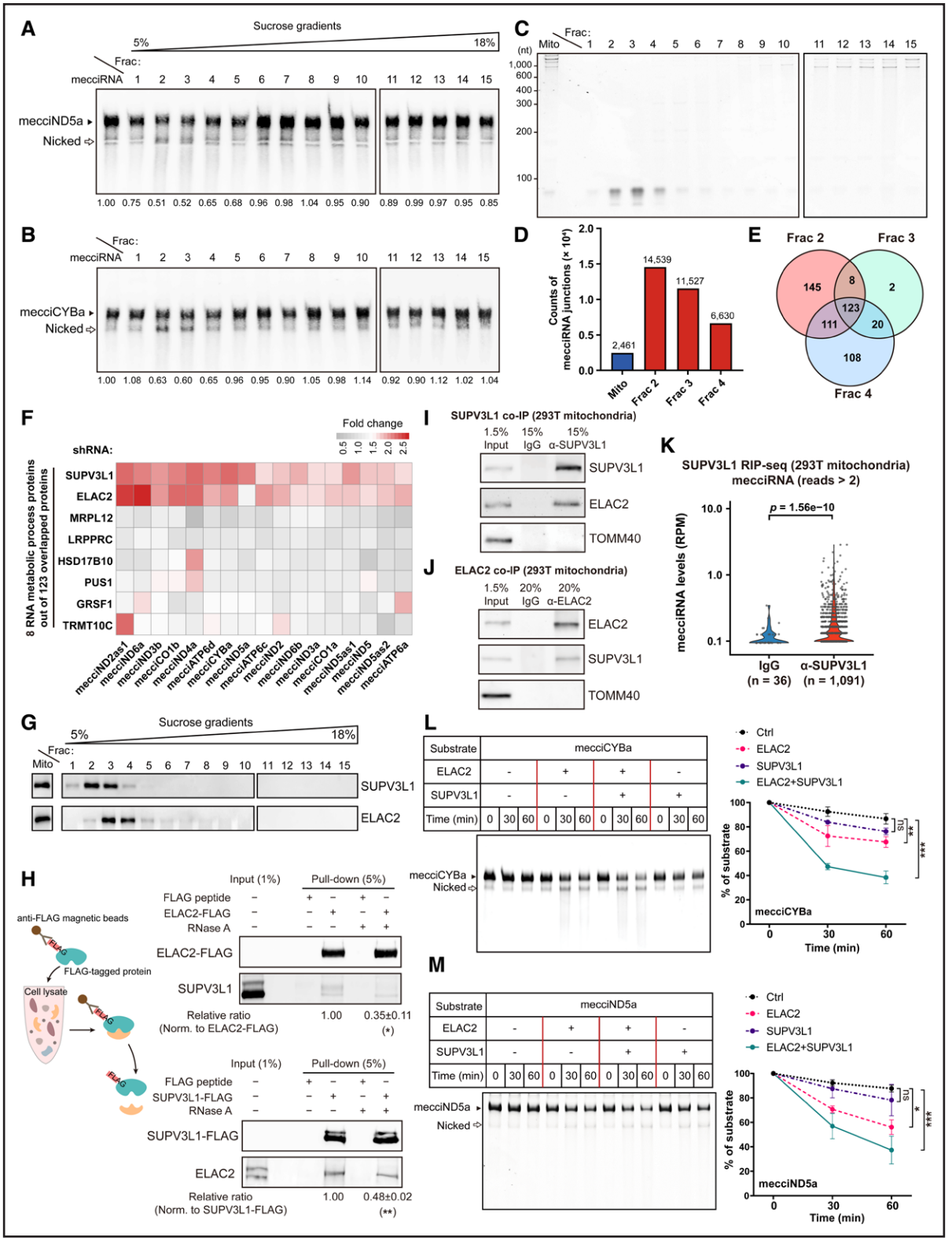

Figure 2. Identification of SUPV3L1 and ELAC2 as a mecciRNA degradation complex.
A and **B**, Gel image of in vitro synthesized biotin-labeled mecciND5a (**A**) and mecciCYBa (**B**) incubated with mitochondrial fractions from a 5% to 18% sucrose gradient. The open arrow represents nicked product of in vitro mecciRNA synthesis. The quantification of mecciRNA bands in each fraction (Frac; relative to the substrate, the first lane) is indicated under the gel. **C**, RNA gel separation of RNAs from mitochondrial sucrose gradient fractions. Mito, total mitochondrial RNAs. **D**, Numbers of reads mapped to mecciRNA junctions from small RNA sequencing of sucrose gradient fractions (Frac) 2–4. **E**, Venn diagram of proteins identified from mass spectrometry (MS) in Frac 2–4. **F**, Heatmap of relative levels of mecciRNAs under the knockdown of 8 proteins in mitochondrial RNA metabolic process with shRNAs in 293T cells. The levels of (*Continued*)

Figure 2 Continued. individual mecciRNA were analyzed with RT-qPCR, and fold changes were calculated relative to the negative control shRNA. **G**, Western blots of SUPV3L1 and ELAC2 in indicated mitochondrial sucrose gradient fractions (Frac) from 293T cells. Mito, whole mitochondrial proteins. **H**, Schematic illustration of protein pull-down assay using recombinant FLAG-tagged human SUPV3L1 and ELAC2 proteins with 293T cell lysate (**left**). The interaction between SUPV3L1 and ELAC2 with or without RNase A treatment is shown by Western blots (**right**). FLAG peptide was used as a negative control. The relative amount of SUPV3L1 or ELAC2 pulled down is labeled under the image. **I** and **J**, Coimmunoprecipitation (co-IP) showing the interaction of SUPV3L1 and ELAC2 with 293T mitochondrial materials. TOMM40, a mitochondrial marker and a negative control of co-IP. **K**, Violin plot shows the enrichment of mecciRNAs (reads >2) from RNA immunoprecipitation sequencing (RIP-seq) of SUPV3L1 in 293T mitochondria. Numbers of mecciRNAs are indicated as n numbers. **L** and **M**, In vitro degradation assays of synthesized mecciCYBa (**L**) and mecciND5a (**M**) by recombinant ELAC2 and recombinant SUPV3L1 protein. Graphs show quantified substrate degradation at the corresponding time point. In **H**, **L**, and **M**, data are shown as mean±SEM from 3 independent experiments. *P* values were from 2-tailed paired Student *t* test (**H**), 2-tailed Wilcoxon rank-sum test (**K**), and 2-way ANOVA followed by 2-tailed Dunnett multiple-comparisons test (**L** and **M**). ns, not significant; **P*<0.05; ***P*<0.01; ****P*<0.001. shRNA, short hairpin RNA.

of exogenous mecciRNAs had significant therapeutic effects on HF mice.

METHODS

The data, protocols, and study materials will be made available to other researchers for purposes of reproducing the results or replicating the procedures. Detailed methods and supporting data are available in the Supplemental Material.

Experimental Animals

All experiments involving mice were approved by the biomedical research ethics committee of the University of Science and Technology of China and are compliant with the National Institutes of Health *Guide for the Care and Use of Laboratory Animals*.

Statistical Analysis

The statistical significance was evaluated by 2-tailed Student *t* test for data between data of 2 groups that follow the normal distribution. Two-way ANOVA was used for comparisons among >2 groups. Nonparametric tests such as the 2-tailed Wilcoxon rank-sum test (or Mann-Whitney *U* test) and the Kolmogorov-Smirnov test were used to evaluate the statistical significance as indicated in the figure legends. The statistical graphs were generated by GraphPad Prism 9 or R software.

RESULTS

MecciRNAs Are Fast Degraded

To assess the stability of mecciRNAs, we treated cells with actinomycin D (ActD) to inhibit the transcription in both mitochondria and nuclei. The global mecciRNA levels in mitochondria decreased significantly upon transcriptional inhibition in human 293T, HeLa, and mouse N2a cell lines (Figure S1A through S1H; Supplemental Data S1). In line with many previous studies, the global nuclear genome–encoded circRNA (ng-circRNA) levels were not significantly decreased (Figure S1A through S1H; Supplemental Data S1). Ng-circRNAs even demonstrated a slight but significant increase after 2 h ActD treatment, which might be a result of the degradation of other types of RNAs that increased the relative abundance of ng-circRNAs, or ng-circRNAs were still generated from linear precursors (Figure S1B, S1D, and S1G). Global levels of nuclear-encoded linear RNAs showed significant but not prominent change (Figure S1I). Levels of the 13 mitochondria-encoded mRNAs showed a similar trend of decrease compared with mecciRNAs (Figure S1J and S1K). A total of 84 ng-circRNAs were identified in mitochondrial RNA sequencing data, and their levels in the mitochondria of 293T cells did not decrease after ActD treatment (Figure S1L).

Levels of 5 mecciRNAs and 5 ng-circRNAs were experimentally examined after ActD treatment in 293T cells (Figure 1A). Rapid reduction of all the mecciRNAs was observed with a half-life of approximately 4 hours, whereas ng-circRNAs examined remained stable after 8 h ActD treatment (Figure 1A). Two mecciRNAs and 2 ng-circRNAs were further examined by Northern blot and single-molecule fluorescence in situ hybridization (smFISH), and the levels of both mecciRNAs but not the 2 ng-circRNAs displayed significant decreases (Figure 1B through 1D; Figure S2A and S2B).

Another inhibitor of mitochondrial transcription, ethidium bromide (EtBr), was also applied to further corroborate the fast decay of mecciRNAs. Levels of mecciRNAs but not ng-circRNAs examined were significantly decreased after EtBr treatment (Figure 1E). Northern blots and smFISH also confirmed the 2 mecciRNAs but not ng-circRNAs displayed lower levels in 293T cells after 2 h EtBr treatment (Figure 1F through 1H; Figure S2C).

smFISH of 2 individual mecciRNAs showed that the portion of mecciRNA not colocalizing with mitochondria was unchanged upon ActD or EtBr treatment (Figure S2D). smFISH signals that did not colocalize with mitochondria were presumably from mecciRNAs exported from mitochondria. This result indicated that there might be no significant change in mitochondrial mecciRNA export to contribute to the drastic decreases of mecciRNA levels in mitochondria. ng-circRAPGEF5 and ng-circPKHB were 2 circRNAs that could be identified in mitochondria, and their smFISH signals that colocalized with MitoTracker and their smFISH signals in the whole cell did not show significant change upon either ActD or EtBr treatment (Figure S3A and S3B). Furthermore, we found that the EU-labeled nascent mecciRNAs examined

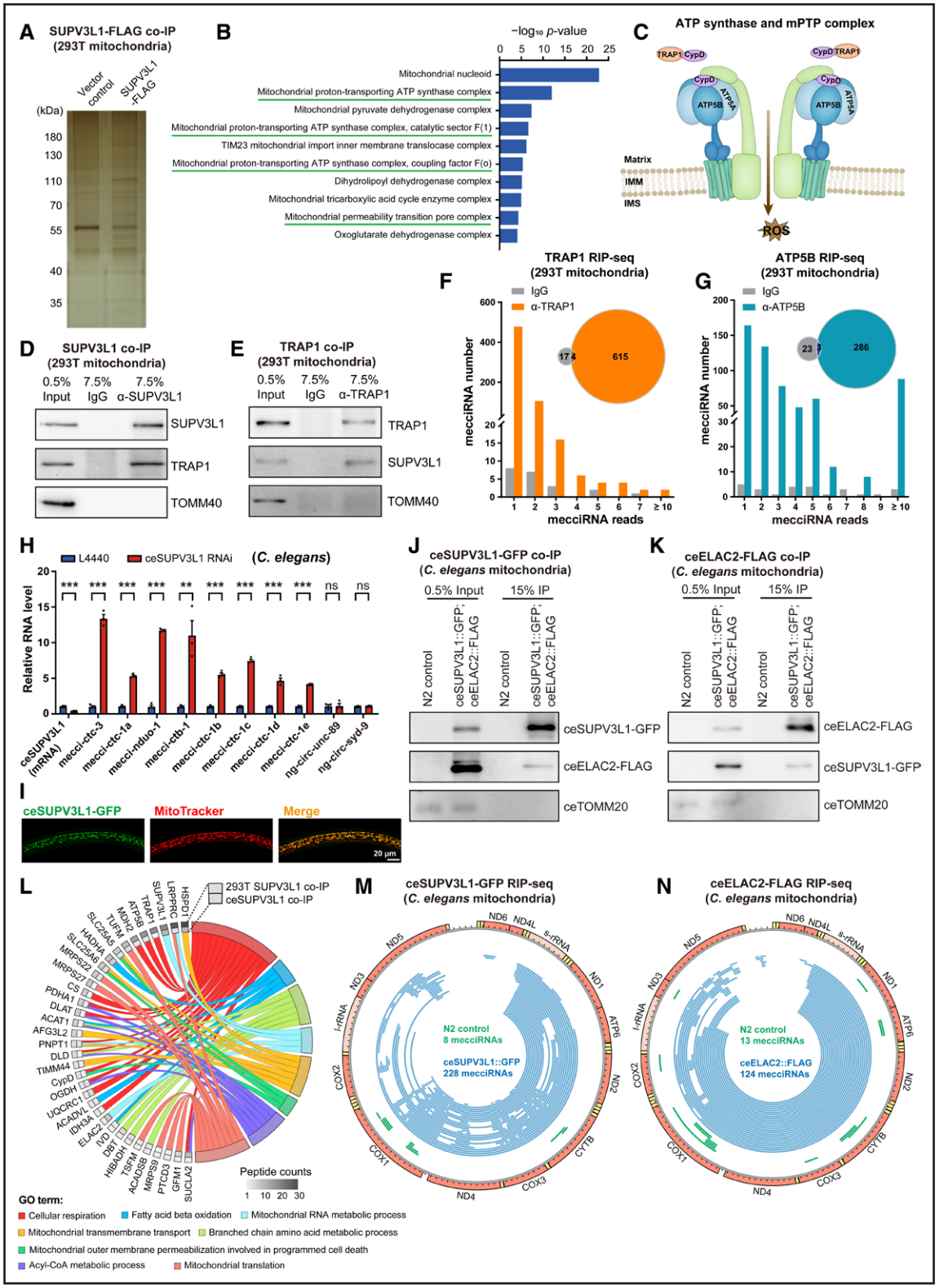

Figure 3. SUPV3L1 and mecciRNAs interact with components and regulators of mPTP, and the mecciRNA degradation mechanism is conserved in animals.

A, co-IP of SUPV3L1-FLAG in mitochondria from 293T cells transfected with SUPV3L1-FLAG overexpression plasmid. The proteins were subjected to silver staining. Vector control, empty vector. **B**, Gene Ontology (GO) analysis of the 159 proteins identified from SUPV3L1 co-IP by MS. **C**, Schematic depicting the mitochondrial permeability transition pore (mPTP) complex and its regulators. The proteins identified in SUPV3L1 co-IP are indicated. **D** and **E**, co-IP showing the interaction of SUPV3L1 and TRAP1 in 293T mitochondria. TOMM40, negative control. **F** and **G**, RIP-seq of TRAP1 (**F**) and ATP5B (**G**) in 293T mitochondria. Histograms show the read distribution of mecciRNAs, and (*Continued*)

Figure 3 Continued. Venn diagrams demonstrate the numbers of mecciRNAs immunoprecipitated by the corresponding antibodies. **H,** RT-qPCR detection of ceSUPV3L1 mRNA, mecciRNAs, and ng-circRNAs in *Caenorhabditis elegans* (young adult) under feeding RNAi to knockdown ceSUPV3L1. L4440, negative control of feeding RNAi. **I**, Representative images of ceSUPV3L1-GFP location in *ceSUPV3L1::GFP; ceELAC2::FLAG C elegans* (young adult). Both ceSUPV3L1-GFP and ceELAC2-FLAG were expressed as endogenous fusion proteins. Mitochondria were stained by MitoTracker. **J** and **K**, co-IP showing the interaction of ceSUPV3L1 and ceELAC2 in mitochondria from *ceSUPV3L1::GFP; ceELAC2::FLAG C elegans* (young adult). ceTOMM20, negative control. **L**, GO analysis of 41 overlapped proteins from human SUPV3L1 co-IP and ceSUPV3L1-GFP co-IP. The protein peptide counts identified by MS are shown with gray scale, and GOs are shown with different colors. **M** and **N**, Circos plots represent RIP-seq of endogenous fusion of ceSUPV3L1 (**M**) and ceELAC2 (**N**) in mitochondria from *ceSUPV3L1::GFP* and *ceELAC2::FLAG C elegans* (young adult). The start site and end site of each mecciRNA detected are connected by a line. Mitochondrial DNA-encoded genes are shown on the outer circle. Numbers of mecciRNAs pulled down are labeled. In **H**, data are shown as mean±SEM; n=3 independent experiments; *P* values were from 2-tailed unpaired Student *t* test. ns, not significant; $^{**}P<0.01$; $^{***}P<0.001$.

were decreased, instead, the EU-labeled ng-circRNAs did not show significant changes after chasing for 2 h (Figure S3C). Collectively, these results demonstrated that mecciRNAs in general were quickly degraded in human and mouse cells.

SUPV3L1 and ELAC2 Are Identified to Participate in MecciRNA Degradation

Degradation assays with sucrose gradient fractions of purified mitochondria and in vitro synthesized mecciRNAs were then performed (Figure S4A and S4B). Prominent degradation of both mecciND5a and mecciCYBa in the 2–4 fraction was observed (Figure 2A and 2B). The highest intensity of small RNA bands was also present in fractions 2 through 4 (Figure 2C). Thousands of small RNA reads annotated to mecciRNA junctions were identified in fractions 2–4, along with small RNAs consisting of tRNAs and also other reads distributed across the whole mitochondrial genome (Figure 2D; Figure S4C). Totals of 387, 153, and 362 confident mitochondrial proteins were detected by mass spectrometry in fractions 2, 3, and 4, respectively, with 123 proteins shared in the 3 fractions (Figure 2E; Supplemental Data S2). These shared proteins were mostly involved in mitochondrial transport and metabolic processes (Figure S4D). A total of 12 of the 123 proteins were mitochondrial RNA metabolic proteins, of which 8 proteins were reported or predicted to regulate RNA expression, and 4 were aminoacyl-tRNA synthetases (Figure S4E).[21] It was found that knockdown of the helicase SUPV3L1 or the endonuclease ELAC2 significantly elevated levels of all 17 mecciRNAs experimentally examined (Figure 2F). Both SUPV3L1 and ELAC2 were present in the mitochondrial fractions 2–4 (Figure 2G). In summary, these results identified SUPV3L1 and ELAC2 as factors participating in the degradation of mecciRNAs.

SUPV3L1 and ELAC2 Form a Complex to Degrade MecciRNAs

Protein pull-down of in vitro purified FLAG-tagged human SUPV3L1 added into 293T cell lysate could coprecipitate the endogenous ELAC2; pull-down of the exogenous ELAC2-FLAG protein could also coprecipitate the endogenous SUPV3L1 (Figure 2H). Digestion with RNase A decreased the endogenous protein that co-pulled down, indicating that the interaction was facilitated by RNA (Figure 2H). Coimmunoprecipitation (co-IP) analysis revealed that endogenous SUPV3L1 and ELAC2 could pull down each other (Figure 2I and 2J). RNA immunoprecipitation followed by RNA sequencing (RIP-seq) of the endogenous SUPV3L1 with mitochondrial materials or whole cell lysates revealed that hundreds of mecciRNAs but few ng-circRNAs interacted with SUPV3L1 (Figure 2K; Figure S5A and S5B; Supplemental Data S3). RNA immunoprecipitation of ELAC2 could also pull down mecciRNAs but not ng-circRNAs, examined by quantitative reverse transcription polymerase chain reaction (Figure S5C). These results indicated that the helicase SUPV3L1 bound to mecciRNAs and formed a complex with the RNase Z ELAC2. Purified ELAC2 but not SUPV3L1 alone could degrade in vitro synthesized mecciCYBa or mecciND5a, and with the copresence of ELAC2 and SUPV3L1, the degradation of mecciRNAs was significantly enhanced (Figure 2L and 2M; Figures S4A and S5D). Collectively, these results revealed that ELAC2 and SUPV3L1 formed a complex to degrade mecciRNAs.

SUPV3L1 and MecciRNAs Interact With mPTP Components and Regulators

Proteins from SUPV3L1-FLAG co-IP were then identified by mass spectrometry, and 159 confident mitochondrial proteins were identified (Figure 3A; Supplemental Data S2). ELAC2 along with known interacting proteins such as PNPase was identified (Supplemental Data S2).[20] SUPV3L1 binding proteins were enriched mostly for the Gene Ontology term mitochondrial nucleoid, and it has been known that multiple RNA binding proteins copurify with the nucleoid (Figure 3B).[22] The next enriched Gene Ontology terms were mainly related to mitochondrial membrane-associated protein complexes, such as ATP synthase complex and mPTP complex (Figure 3B). Besides ATP synthesis, subunits of ATP synthase also participate in the formation and regulation of mPTP.[23,24] mPTP regulators TRAP1 (TNF [tumor necrosis factor] receptor–associated protein 1) and CypD (cyclophilin D), along with ATP5A and ATP5B, which are shared

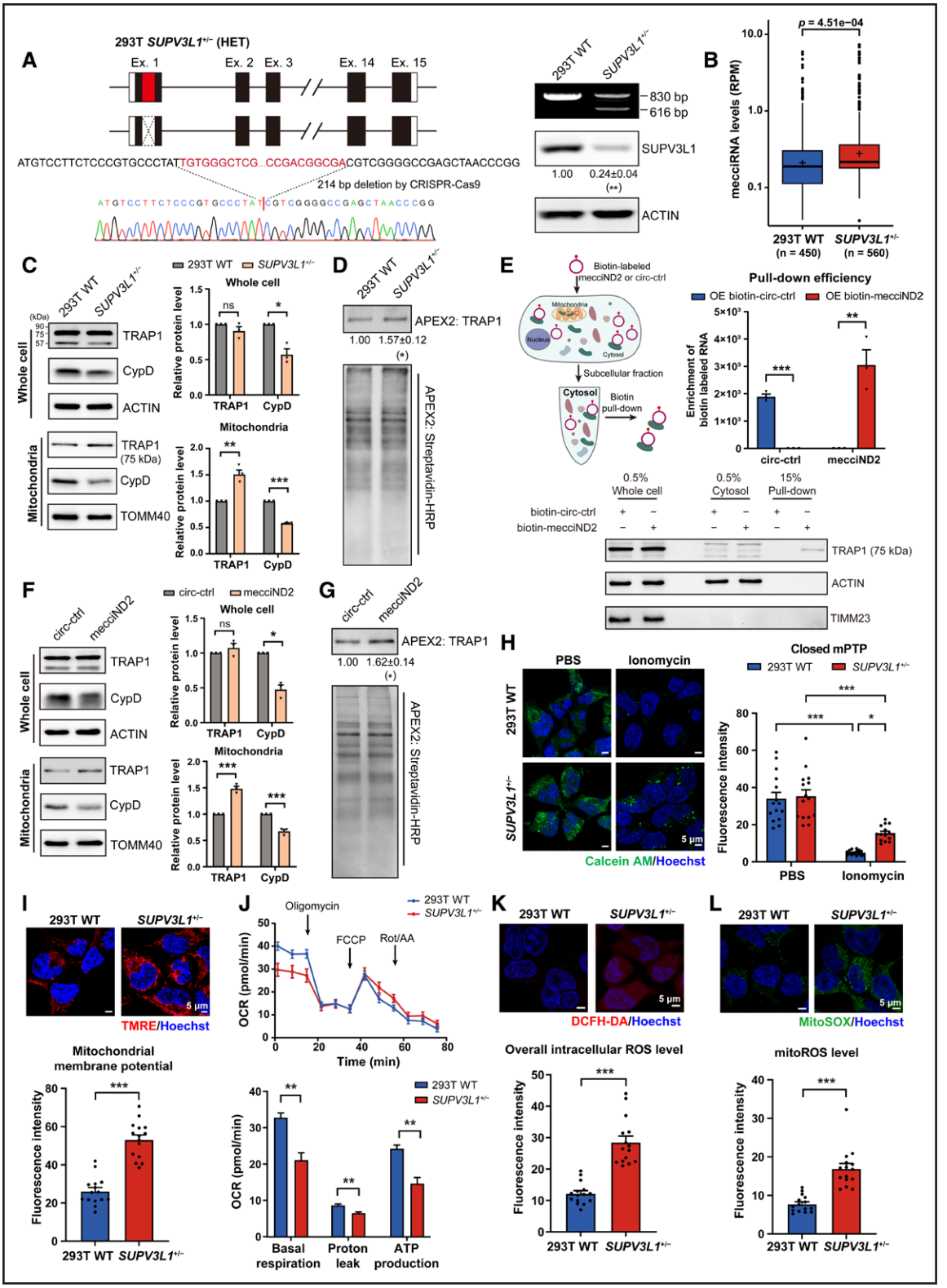

Figure 4. MecciRNAs and mPTP state in *SUPV3L1*$^{+/-}$ cells.

A, Scheme for generating the 293T *SUPV3L1*$^{+/-}$ heterozygote (HET) cells by CRISPR-Cas9. The genome editing site of *SUPV3L1* was confirmed by Sanger sequencing. Genomic PCR of *SUPV3L1* and Western blots of SUPV3L1 protein are shown. Relative level of SUPV3L1 protein in 293T *SUPV3L1*$^{+/-}$ cells is shown. **B**, RNA-seq of mitochondrial RNA from 293T WT and *SUPV3L1*$^{+/-}$ cells. Box plot shows the mecciRNA level in each group. MecciRNAs with reads ≥5 in at least one sample were analyzed. Mean, median, interquartile range (IQR), minimum, and maximum reads are shown. The number of mecciRNAs is indicated as the n number. **C**, Whole-cell levels and mitochondrial levels of TRAP1 and CypD in 293T WT and *SUPV3L1*$^{+/-}$ cells examined by Western blots. The TRAP1 (≈75 kDa) antibody also detected the other (*Continued*)

Figure 4 Continued. HSP90 in whole-cell samples. Quantification is shown with bar graph. ACTIN and TOMM40, loading controls of the whole cell and mitochondrial proteins, respectively. **D**, 293T WT and *SUPV3L1*$^{+/-}$ cells overexpressing an engineered mitochondrial matrix located ascorbate peroxidase (matrix-APEX2) were used to enrich biotinylated mitochondrial proteins. The APEX2-catalyzed biotinylated TRAP1 (APEX2: TRAP1) level in mitochondria was analyzed by Western blots. The quantification of mitochondrial APEX2: TRAP1 (normalized to the overall biotinylated mitochondrial proteins) is shown. **E**, Biotin-labeled mecciND2 pull-down assay with 293T cytosolic materials. Biotin-circ-ctrl, a biotin-labeled circularized fragment (≈250 nt) of *gfp*. Pull-down efficiency was detected by RT-qPCR. TRAP1 co–pulled down with mecciND2 was verified by Western blotting. The TRAP1 (≈75 kDa) antibody also detected the other HSP90 in whole cell samples and cytosol samples. ACTIN and TIMM23 served as cytosolic and mitochondrial markers, respectively. **F**, Western blots and the quantification of TRAP1 and CypD at whole cell level and mitochondrial level in 293T cells, transfected with circ-ctrl or mecciND2. Circ-ctrl, in vitro synthesized circularized fragment of *gfp*. ACTIN and TOMM40, loading controls at the whole cell level or mitochondrial level, respectively. **G**, Mitochondrial TRAP1 levels analyzed by APEX2 assay, with the transfection of in vitro synthesized circ-ctrl or mecciND2 in 293T cells. The quantification of APEX2: TRAP1 (normalized to the overall enriched biotinylated mitochondrial proteins) is shown. **H**, Representative images and quantification of Co^{2+}–Calcein assays in 293T WT and *SUPV3L1*$^{+/-}$ cells. Ionomycin was used to trigger mPTP opening. Closed mPTP is reflected by Calcein AM signals (n=15 cells for each group). **I**, Representative images and quantification of tetramethylrhodamine methyl ester (TMRE) staining of 293T WT and *SUPV3L1*$^{+/-}$ cells. Mitochondrial membrane potential is reflected by TMRE signals (n=15 cells for each group). **J**, Mitochondrial respiration profile of 293T WT and *SUPV3L1*$^{+/-}$ cells. OCR, oxygen consumption rate. Oligomycin (ATP synthase inhibitor), FCCP (membrane potential uncoupler), Rotenone (Complex I inhibitor), and Antimycin A (AA, Complex III inhibitor). Levels of basal respiration, proton leak, and ATP production are calculated based on the OCR curve. **K**, Representative images of dichloro-dihydro-fluorescein diacetate (DCFH-DA) staining of 293T WT and *SUPV3L1*$^{+/-}$ cells. DCFH-DA signals reflecting the overall intracellular ROS were quantified. n=15 cells for each group. **L**, Representative images of MitoSOX staining of 293T WT and *SUPV3L1*$^{+/-}$ cells. MitoSOX signals reflecting mitochondrial ROS were quantified (n=15 cells for each group). Scale bars are labeled in microscopy images. In **A** and **C** through **G**, data are mean±SEM from 3 independent experiments. In **B**, one biological sample for each cell line was sequenced. In **J**, data are mean±SEM from 5 experimental replicates for each cell line. *P* values were from 2-tailed paired Student *t* test (**A**, **C**, **D**, **F**, and **G**), 2-tailed Wilcoxon rank-sum test (**B**), 2-way ANOVA followed by Bonferroni post hoc test (**H**), and 2-tailed unpaired Student *t* test (**E** and **I** through **L**). ns, not significant; **P*<0.05; ***P*<0.01; ****P*<0.001.

components of ATP synthase complex and mPTP, were identified (Figure 3C; Supplemental Data S2). The permeability of mPTP is regulated by CypD, which interacts with ATP synthase subunits such as ATP5B to promote the opening of mPTP, whereas TRAP1, a key mitochondrial HSP90 chaperone, binds to CypD to block the interaction between CypD and ATP synthase subunits.[25–28] The interaction between TRAP1 and CypD was confirmed (Figure S5E). Co-IP with mitochondrial materials confirmed the interaction between SUPV3L1 and TRAP1 (Figure 3D and 3E). RIP-seq demonstrated that 619 mecciRNAs were enriched by TRAP1 (Figure 3F; Figure S5F and S5G; Supplemental Data S3). A total of 289 mecciRNAs were precipitated by ATP5B examined with RIP-seq (Figure 3G; Figure S5F and S5G; Supplemental Data S3). TRAP1 bound to more species of mecciRNAs than ATP5B, and the 2 proteins associated with distinct sets of mecciRNAs (Figure S5G). TRAP1 tended to bind to mecciRNAs with medium GC content (peaked around ≈44% GC) and a wide range of lengths, whereas ATP5B-associated mecciRNAs were more dispersed in GC contents and were shorter in length (peaked around ≈300 nt; Figure S5H and S5I). These results demonstrated that SUPV3L1 and mecciRNAs interacted with mPTP components such as ATP5B and regulators such as TRAP1.

MecciRNA Degradation Mechanism Is Conserved in *Caenorhabditis elegans*

SUPV3L1 and ELAC2 protein sequences are highly conserved in animals (Figure S6A). Feeding RNAi of ceSUPV3L1 (*C08F8.2* in *C elegans*) led to significantly increased levels of mecciRNAs (Figure 3H). Knockdown of ceSUPV3L1 decreased the mecciRNA degradation upon the treatment of ActD for 6 hours (Figure S6B and S6C). Endogenous ceSUPV3L1-GFP fusion was observed to colocalize with mitochondria (Figure 3I; Figure S6D). When ceSUPV3L1-mCherry and ceELAC2-mCherry were expressed in human 293T cells, the cytoplasmic portion of both proteins colocalized with mitochondria (Figure S6E). Immunoprecipitation was conducted against the endogenous ceSUPV3L1-GFP or ceELAC2-FLAG, and both proteins could co-IP each other in *C elegans* (Figure 3J and 3K; Figure S6D). Proteins from ceSUPV3L1-GFP co-IP were subsequently analyzed by mass spectrometry, and 71 mitochondrial proteins were identified (Figure S6F; Supplemental Data S2). After overlapping with human SUPV3L1 binding proteins, 41 conserved proteins were discovered, including ELAC2, TRAP1, ATP5B, and CypD (Figure S6G). These 41 proteins were enriched in 8 biological processes including the mitochondrial RNA metabolic process, mitochondrial transmembrane transport, and mitochondrial outer membrane permeabilization (Figure 3L). ceSUPV3L1 and ceELAC2 bound to hundreds of mecciRNAs in *C elegans* mitochondria (Figure 3M and 3N; Supplemental Data S3). Collectively, these results indicated that mecciRNAs were degraded by SUPV3L1/ELAC2 complex, and many proteins that interacted with this complex might be conserved from *C elegans* to mammals.

MecciRNAs Increase Mitochondrial TRAP1 and Shut Down mPTP

We then generated a heterozygous SUPV3L1 293T cell line (293T *SUPV3L1*$^{\pm}$, or 293T HET) using CRISPR-Cas9 (Figure 4A; Figure S7A). The overall mecciRNA but

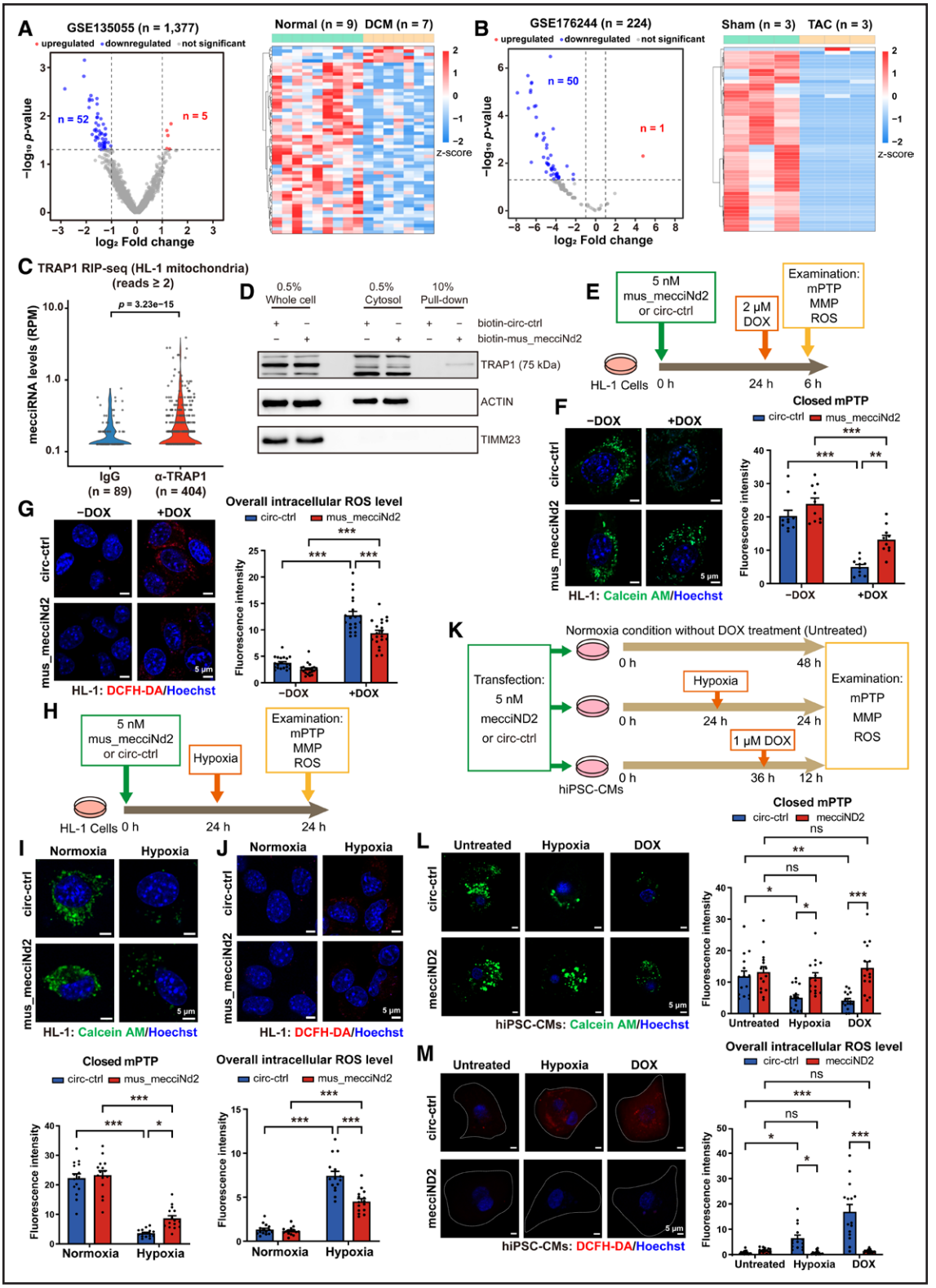

Figure 5. MecciRNAs are downregulated in failing hearts, and mecciND2 protects cultured mouse and human cardiomyocytes from deleterious mtROS.

A, Volcano plot and heatmap revealing differential changes of mecciRNAs in left ventricular heart tissue from 7 patients with heart failure (HF) diagnosed as dilated cardiomyopathy (DCM) and 9 healthy donors from published RNA-seq data (GSE135055; see Supplemental Methods for details). Blue and red dots represent significantly downregulated ($P<0.05$ and $\log_2$ fold change <-1) and upregulated ($P<0.05$ and $\log_2$ fold change >1) mecciRNAs, respectively. **B**, Volcano plot and heatmap revealing differential changes of mecciRNAs in mouse failing hearts (3 vs 3) from published RNA-seq data (GSE176244). Blue and red dots represent significantly downregulated ($P<0.05$ and $\log_2$ fold change <-1) and upregulated ($P<0.05$ and $\log_2$ fold change >1) mecciRNAs, respectively. TAC, transverse aortic constriction, a mouse model for (*Continued*)

Figure 5 Continued. pressure overload-induced heart failure. Sham, control mice underwent the identical surgical procedure without aortic constriction. **C**, Violin plot shows the enrichment of mecciRNAs (reads ≥2) from RIP-seq of TRAP1 in HL-1 mitochondria. Numbers of mecciRNAs are indicated as n numbers; 1 pair of IgG and α-TRAP1 samples were sequenced. α-, antibody. *P* values were from 2-tailed Wilcoxon rank-sum test. **D**, Biotin-labeled mus_mecciND2 pull-down assay with HL-1 cytosolic materials. Biotin-circ-ctrl, a control of biotin-labeled circularized fragment (≈250 nt) of *gfp*. TRAP1 co–pulled down was verified by Western blots. ACTIN and TIMM23 served as cytosolic and mitochondrial marker, respectively. The TRAP1 (≈75 kDa) antibody also detected the other HSP90 in whole cell samples and cytosol samples. **E**, Workflow for the application of in vitro synthesized mus_mecciNd2 in HL-1 cells under DOX treatment. Circ-ctrl, In vitro synthesized circularized fragment of *gfp*. MMP, mitochondrial membrane potential. **F**, Representative images of Co^{2+}–Calcein assays (without adding ionomycin to trigger mPTP opening) in HL-1 cells transfected with circ-ctrl or mus_mecciNd2, with or without DOX treatment for 6 h. Closed mPTP is reflected by Calcein AM signals (n=10 cells per group). **G**, Representative images and the quantification of overall intracellular ROS (DCFH-DA staining) in HL-1 cells transfected with circ-ctrl or mus_mecciNd2, with or without DOX treatment for 6 h (n=20 cells per group). **H**, Workflow for the application of in vitro synthesized mus_mecciNd2 in HL-1 cells under hypoxia treatment. **I** and **J**, Representative images and quantification of closed mPTP (Co^{2+}–Calcein assays; **I**) and overall intracellular ROS (DCFH-DA staining; **J**) in HL-1 cells transfected with circ-ctrl or mus_mecciNd2 under normoxia or hypoxia for 24 h (n=15 cells per group). **K**, Workflow for the application of in vitro synthesized mecciND2 in hiPSC-CMs under normal conditions (untreated), hypoxia, or DOX treatment. **L** and **M**, Representative images and quantification of closed mPTP (Co^{2+}–Calcein assays; **L**) and overall intracellular ROS (DCFH-DA staining; **M**) in hiPSC-CMs transfected with circ-ctrl or mecciND2 under hypoxia (for 24 h) or DOX (12 h) treatment (n=15 cells per group). Scale bars are labeled in the microscopy images. In **F**, **G**, **I**, **J**, **L**, and **M**, data are shown as mean±SEM. *P* values were from 2-way ANOVA followed by Bonferroni post hoc test. ns, not significant; **P*<0.05; ***P*<0.01; ****P*<0.001.

not the ng-circRNA levels were significantly increased in 293T HET cells compared with WT cells (Figure 4B; Figure S7B and S7C; Supplemental Data S4). EU pulse-chasing demonstrated that the examined mecciRNAs were degraded slower in HET cells (Figure S7D).

The whole-cell levels of TRAP1 were relatively unchanged, whereas the mitochondrial levels of TRAP1 were significantly increased in the HET cells (Figure 4C). Both whole-cell and mitochondrial levels of CypD were significantly decreased (Figure 4C). APEX2 methodology that promptly labels mitochondrial matrix proteins with biotin revealed that mitochondrial TRAP1 levels were increased in 293T HET cells (Figure 4D).[29,30]

We then transfected in vitro synthesized biotinylated mecciND2 (biotin-mecciND2) into the WT cells (Figure 4E). A biotinylated circRNA with *gfp* sequences was used as a negative control. MecciND2 was among the top 5 enriched mecciRNAs in TRAP1 RIP-seq (Figure 3F), and *C elegans* ND2 also encoded a mecciRNA that was identified in ceSUPV3L1 RIP-seq (Figure 3M). The exogenous mecciND2 interacted with TRAP1 in the cytosol (Figure 4E). Application of exogenous mecciND2 increased the TRAP1 levels in the mitochondria, whereas the whole cell levels of TRAP1 were not significantly altered (Figure 4F and 4G; Figure S7E). Whole-cell and mitochondrial levels of CypD were significantly decreased upon the application of mecciND2 (Figure 4F). These results demonstrated that exogenous mecciND2 could interact with cytosolic TRAP1 and lead to changes in the whole cell as well as mitochondrial levels of TRAP1 and CypD.

Compared with WT cells, HET cells exhibited significantly higher Calcein AM fluorescence, indicating that a larger proportion of mPTP remained in a closed state (Figure 4H). Elevated membrane potential of HET cell mitochondria was observed, reflecting a more closed state of mPTP (Figure 4I). Significantly decreased basal respiration, ATP production, and proton leak of HET cells compared with WT cells were observed with oxygen consumption rate assays (Figure 4J). The decreased proton leak was consistent with a more closed state of mPTP in the HET cells.[31] Significantly increased whole cell ROS and mtROS levels were found in the HET cells (Figure 4K and 4L). These results demonstrated that SUPV3L1 insufficiency led to increased mecciRNA levels, higher mitochondrial levels of TRAP1, and lower mitochondrial and total levels of CypD, and resulted in a more closed state of mPTP. The ROS levels were still increased, not fully restrained by the closed state of mPTP in the HET cells, very possibly because of the multifunctional nature of SUPV3L1, which led to decreased basal respiration and ATP production that caused higher ROS generation.[32]

Mus_mecciNd2 Protects Cardiomyocytes Against Induced mPTP Opening

Proteins purified by SUPV3L1 co-IP were evaluated in the database of gene-disease associations (DisGeNET),[33] and cardiomyopathy was one of the highly related diseases (Figure S7F). From published RNA sequencing data of heart from patients with HF [34] or mouse a model,[35] changes in mecciRNA levels were revealed (Figure 5A and 5B; Supplemental Data S5). Bioinformatics analyses of RNA sequencing of left ventricles (LVs) from 7 dilated cardiomyopathy patients with HF and 9 normal people found 52 downregulated and 5 upregulated mecciRNAs (Figure 5A). A total of 50 downregulated and 1 upregulated mecciRNAs were identified from 3 pairs of sham control and transverse aortic constriction (TAC) mice (Figure 5B; Figure S7G). TAC in mice is a common model for pressure overload–induced cardiac insufficiency, left ventricular dilatation, and eventually HF.[36]

We first treated murine HL-1 cardiomyocyte cell line with DOX or hypoxia. Both conditions are known to trigger or aggravate HF.[37,38] Under either DOX or hypoxia treatment, lower levels of mecciRNAs and higher SUPV3L1 and ELAC2 levels were revealed (Figure S7H through S7K). The relative amount of mtDNA was slightly but

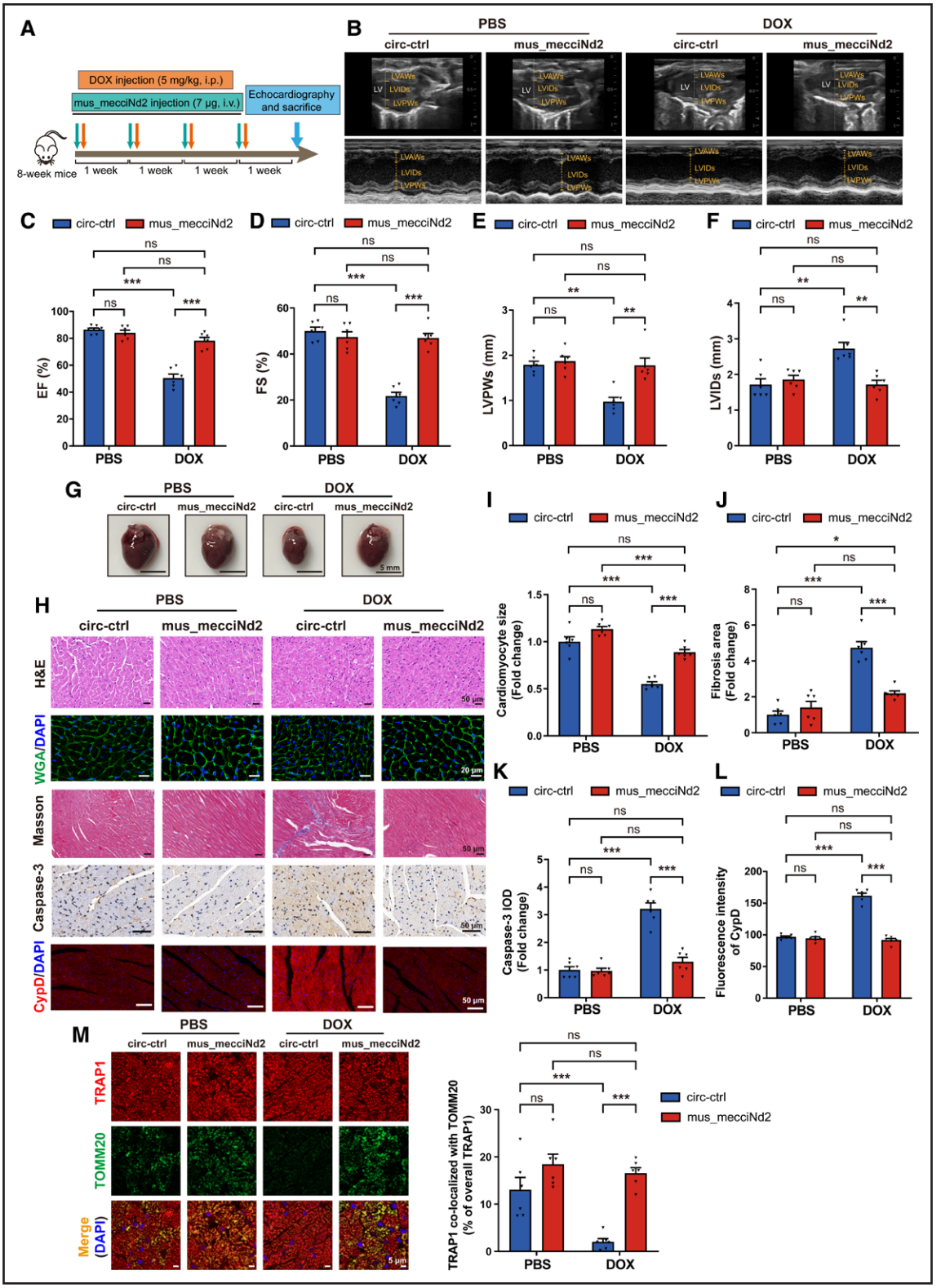

Figure 6. Mus_mecciNd2 demonstrates protective effects in doxorubicin-induced heart failure.
A, Schedule of the construction of DOX-induced mouse models of heart failure (HF) and administration of mus_mecciNd2. **B**, Representative B-mode and M-mode echocardiographic images after circ-ctrl or mus_mecciNd2 application in mice with or without DOX treatment. PBS, the vehicle for DOX. Left ventricular (LV), left ventricular posterior wall end-systole (LVPWs), left ventricular anterior wall end-systole (LVAWs), and left ventricular internal diameter end-systole (LVIDs) are indicated. **C** through **F**, Cardiac function reflected by ejection fraction (EF%), fractional shortening (FS%), left ventricular posterior wall end-systole (LVPWs), and left ventricular internal diameter end-systole (LVIDs) measured by echocardiography in circ-ctrl and mus_mecciNd2-injected mice with or without DOX treatment. **G**, Representative photographs of (*Continued*)

Figure 6 Continued. intact heart from circ-ctrl and mus_mecciNd2-treated mice with or without DOX treatment. **H** through **L**, Representative images and the corresponding quantification of hematoxylin and eosin (H&E) staining and wheat germ agglutinin (WGA, green) staining of heart cross-sections. WGA staining images were used for measuring cardiomyocyte sizes (**H** and **I**). Representative images and the quantification of Masson trichrome staining to evaluate fibrosis area (**H** and **J**), Caspase-3 IHC (**H** and **K**), and CypD immunofluorescence (IF) staining (**H** and **L**) of heart cross-sections from circ-ctrl and mus_mecciNd2-treated mice with or without DOX treatment. IOD, integrated optical density of nuclear signal of Caspase-3 measured by ImageJ. **M**, Representative images and the quantification of TRAP1 and TOMM20 IF of heart cross-sections from circ-ctrl and mus_mecciNd2-treated mice with or without DOX treatment. The ratio of TRAP1 signals overlapping with TOMM20 was quantified. The quantification details are included in Supplemental Methods. Data are shown with mean±SEM (n=6 mice per group). *P* values were calculated by 2-way ANOVA followed by Bonferroni post hoc test. ns, not significant; **P*<0.05; ***P*<0.01; ****P*<0.001. Scale bars are labeled in the corresponding images.

significantly increased (≈30%) under hypoxia treatment, and was slightly but significantly decreased (≈20%) under DOX treatment (Figure S7L). These results indicated that there was no drastic decrease in mitochondria content to cause the significant reduction in mecciRNA levels. We tested whether the application of exogenous mus_mecciNd2 could benefit HL-1 cells from the toxicity of DOX. Mus_mecciNd2 was the shortest in length among the top 15 downregulated mecciRNAs in the HF mice (Figure 5B; Figure S7G) and was also enriched by TRAP1 RIP-seq (Figure 5C; Figure S7M; Supplemental Data S3). The short length might facilitate in vitro synthesis. Mus_mecciNd2 and human mecciND2 were predicted to have a large portion of single-stranded regions, which possess similar TRAP1 binding sites (Figure S8A through S8D). Application of in vitro synthesized mus_mecciNd2 to HL-1 cells resulted in lower overall CypD levels, higher mitochondrial levels of TRAP1, and more closed mPTP (Figure S9A through S9D). Pull-down of biotin-mus_mecciNd2 revealed that exogenous mus_mecciNd2 interacted with TRAP1 in the cytosol (Figure 5D; Figure S9E). The application of mus_mecciNd2 antagonized the DOX effect in mPTP opening (Figure 5E and 5F). Consistent with the change in the mPTP state, the application of mus_mecciNd2 also elevated the membrane potential of HL-1 cells under DOX treatment (Figure S9F). DOX has been reported to induce mPTP opening and mtROS release.[39] The overall ROS induced by DOX treatment were significantly reduced under the mus_mecciNd2 application (Figure 5G). Application of mus_mecciNd2 also inhibited mPTP opening, maintained mitochondrial membrane potential, and reduced the overall ROS in HL-1 cells under hypoxia treatment (Figure 5H through 5J; Figure S9G). We subsequently evaluated the function of human mecciND2 in human induced pluripotent stem cell–derived cardiomyocytes. Application of in vitro synthesized human mecciND2 protected human induced pluripotent stem cell–derived cardiomyocytes against induced mPTP opening, maintained mitochondrial membrane potential, and reduced cellular ROS level under hypoxia or DOX treatments (Figure 5K through 5M; Figures S7E, S9H, and S9I). These results together demonstrated that mecciRNA degradation was enhanced in cardiomyocytes under conditions associated with HF, and the application of exogenous mecciND2 could protect cells from elevated ROS by promoting the more closed state of mPTP in both murine and human cardiomyocytes.

Protective Effects of Mus_mecciNd2 in DOX-Induced HF

In a mouse model of DOX-induced HF,[36] we observed lower levels of mecciRNAs including mus_mecciNd2 as well as higher SUPV3L1 and ELAC2 levels in the heart (Figure S10A through S10C). In vitro synthesized mus_mecciNd2 or the control circRNA (circ-ctrl) encapsulated by liposome was administrated to mice by tail vein injection (Figure 6A; Figure S9A). We examined mus_mecciNd2 levels in different organs including the heart, liver, kidney, muscle, and brain after administration of mus_mecciNd2. Approximately 20-fold on day 1 and ≈17-fold on day 3 increases in mus_mecciNd2 levels were observed in the heart (Figure S10D). The liver (≈13-fold on day 1 and ≈8-fold on day 3) and the kidney (≈10-fold on day 1 and ≈5-fold on day 3) also showed increased mus_mecciNd2 levels (Figure S10D). Muscle and brain showed some overexpression on day 1 (Figure S10D). smFISH results revealed that levels of mus_mecciNd2 were also significantly elevated in cardiomyocytes (Figure S10E and S10F).

Toxicity effects of DOX led to a significant decline in the body weight of mice, regardless of whether they were injected with circ-ctrl or mus_mecciNd2 (Figure S10G). Cardiac function analyses by echocardiography demonstrated a significant reduction in ejection fraction (EF) and fractional shortening (FS) in DOX mice injected with circ-ctrl (Figure 6B through 6D; Figure S10H). EF and FS reflect the contraction function of the heart. Administration of mus_mecciNd2 resulted in normal EF and FS in mice under DOX treatment (Figure 6B through 6D; Figure S10H). Analyses of echocardiography revealed that mus_mecciNd2 application protected the heart from the DOX-induced wall thinning of the LV, reflected by measurements of LV posterior wall end-systole and LV anterior wall end-systole (Figure 6B and 6E; Figure S10H and S10I). The DOX-induced LV dilation was also protected by mus_mecciNd2 treatment, as shown in the evaluation of LV internal diameter end-systole (Figure 6B and 6F; Figure S10H).

The decrease in heart weight and size under DOX treatment was alleviated by mus_mecciNd2 injection

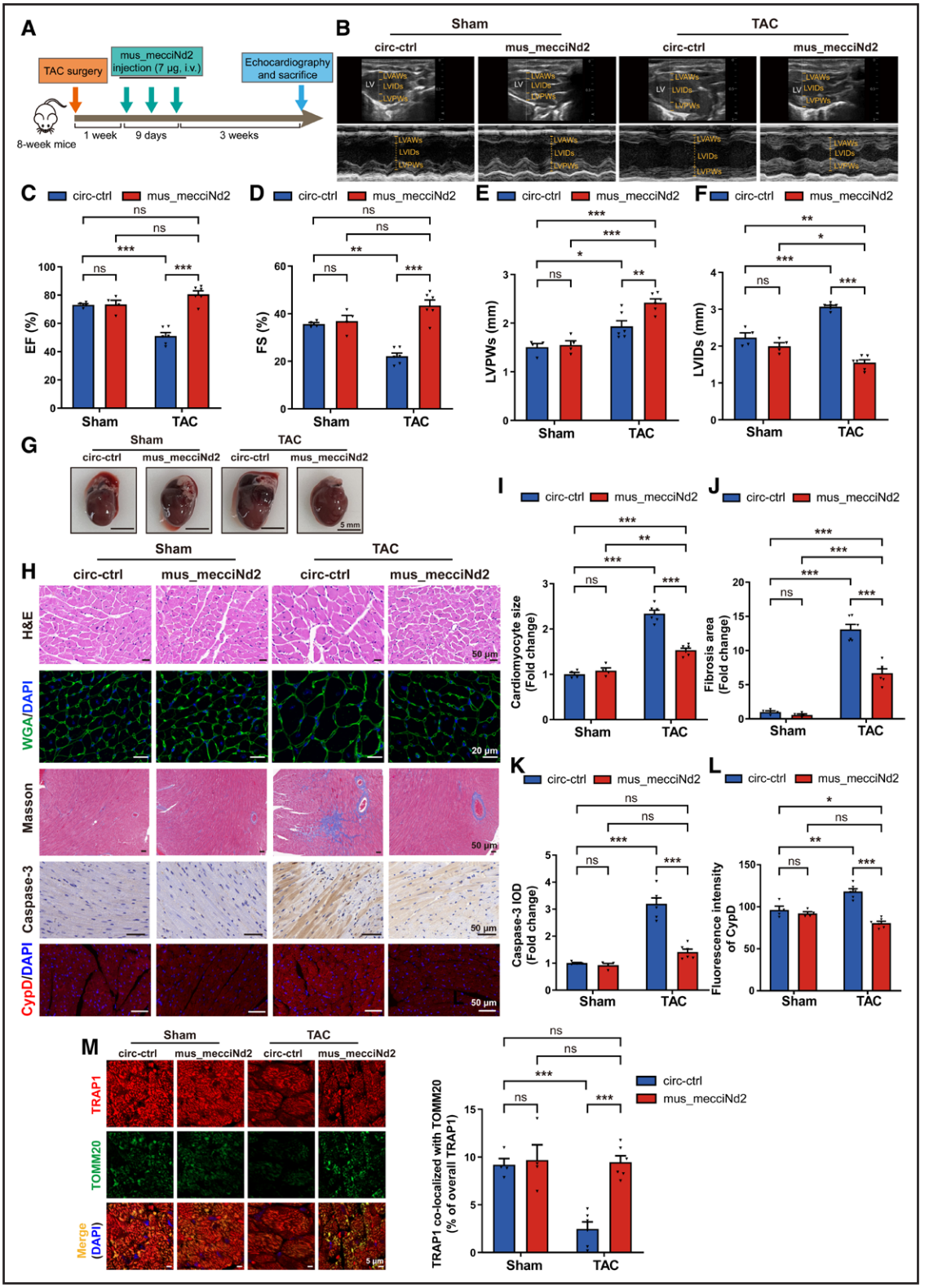

Figure 7. Mus_mecciNd2 demonstrates protective effects in pressure overload–induced heart failure.
A, Schedule of the construction of the TAC surgery in mouse models of heart failure (HF) and administration of mus_mecciNd2. **B**, Representative B-mode and M-mode echocardiographic images of mice with circ-ctrl or mus_mecciNd2 administration in sham or TAC mice. Left ventricular (LV), left ventricular posterior wall end-systole (LVPWs), left ventricular anterior wall end-systole (LVAWs), and left ventricular internal diameter end-systole (LVIDs) are indicated. **C** through **F**, Cardiac function reflected by ejection fraction (EF%), fractional shortening (FS%), left ventricular posterior wall end-systole (LVPWs), and left ventricular internal diameter end-systole (LVIDs) measured by echocardiography in circ-ctrl and mus_mecciNd2-injected mice after sham or TAC surgery. **G**, Representative photographs of intact heart from circ-ctrl and (*Continued*)

Figure 7 Continued. mus_mecciNd2-treated mice after sham or TAC surgery. **H** through **L**, Representative images and the corresponding quantification of hematoxylin and eosin (H&E) staining and wheat germ agglutinin (WGA, green) staining of heart cross-sections. WGA staining images were used for measuring cardiomyocyte sizes (**H** and **I**). Representative images and the quantification of Masson trichrome staining to evaluate fibrosis area (**H** and **J**), Caspase-3 IHC (**H** and **K**), and CypD immunofluorescence (IF) staining (**H** and **L**) of heart cross-sections from circ-ctrl and mus_mecciNd2-treated mice after sham or TAC surgery. IOD, integrated optical density of nuclear signal of Caspase-3 measured by ImageJ. **M**, Representative images and the quantification of TRAP1 and TOMM20 IF of heart cross-sections from circ-ctrl and mus_mecciNd2-treated mice after sham or TAC surgery. The ratio of TRAP1 signals overlapping with TOMM20 was quantified. The quantification details are included in Supplemental Methods. Data are shown with mean±SEM (n=4 mice for sham groups and 6 for TAC groups). *P* values were calculated by 2-way ANOVA followed by Bonferroni post hoc test. ns, not significant; **P*<0.05; ***P*<0.01; ****P*<0.001. Scale bars are labeled in the corresponding images.

(Figure 6G; Figure S10J). Hematoxylin and eosin and wheat germ agglutinin staining revealed that the size of cardiomyocyte was significantly decreased under DOX treatment, and mus_mecciNd2 application prevented this shrinkage (Figure 6H and 6I). Furthermore, cardiac fibrosis induced by DOX was decreased under mus_mecciNd2 treatment (Figure 6H and 6J). Levels of caspase-3 as an apoptosis marker were increased under DOX treatment, and the increase was blocked by mus_mecciNd2 application (Figure 6H and 6K). CypD levels in the heart were significantly increased upon DOX treatment, and mus_mecciNd2 application blocked the increase (Figure 6H and 6L). TRAP1 protein levels were not significantly changed with or without mus_mecciNd2 application, whereas the levels of mitochondrial marker TOMM20 were significantly decreased under DOX treatment (Figure 6M; Figure S10K and S10L). Application of mus_mecciNd2 kept the TOMM20 levels in the DOX-treated heart and preserved the portion of TRAP1 that colocalized with TOMM20 (Figure 6M; Figure S10L). These data supported a protective effect of mus_mecciNd2 administration in cardiomyocytes under DOX toxicity.

Protective Effects of Mus_mecciNd2 in Pressure Overload–Induced HF

To further assess the applicability of mus_mecciNd2, we used another well-established mouse model for pathological cardiac hypertrophy by TAC (Figure 7A).[36] Echocardiography confirmed successful TAC construction (Figure S11A). smFISH results demonstrated elevated levels of mus_mecciNd2 in cardiomyocytes of TAC mice after the injection (Figure S11B). Lower levels of mecciRNAs including mus_mecciNd2 and higher SUPV3L1 and ELAC2 levels were observed in the heart of TAC mice (Figure S11C through S11E).

During the progression of HF induced by elevated left ventricular afterload in the TAC model, the heart experienced a pathological transition from a compensatory phase to a decompensatory phase, ultimately culminating in HF. This process is accompanied by LV remodeling, initially presenting as concentric hypertrophy and subsequently transitioning to eccentric hypertrophy.[40,41] Five weeks after TAC surgery, decreased EF and FS were observed in TAC mice with circ-ctrl injection, whereas EF and FS of mus_mecciNd2-injected mice were superior to those of circ-ctrl–injected mice, and were even comparable with those of the sham group (Figure 7B through 7D; Figure S11F). Significantly elevated LV posterior wall end-systole and LV anterior wall end-systole were observed in both mus_mecciNd2-injected and circ-ctrl–injected TAC mice (Figure 7B and 7E; Figure S11F and S11G), indicating the presence of compensatory hypertrophy of LV in both groups of TAC mice. Mus_mecciNd2-injected mice exhibited higher LV wall thickness but lower LV internal diameter end-systole compared with circ-ctrl–injected mice (Figure 7E and 7F; Figure S11F and S11G), suggesting that the LV of mus_mecciNd2-injected mice remained in the stage of concentric hypertrophy. In contrast, the LV internal diameter end-systole increased significantly in circ-ctrl–injected TAC mice, suggesting that eccentric hypertrophy occurred (Figure 7F; Figure S11F). Based on the echocardiography results, we speculated that mus_mecciNd2 conferred cardioprotective effects, prolonged the compensatory phase, and delayed the transition to decompensation, whereas the circ-ctrl–injected TAC mice already progressed into the decompensatory phase.

The body weight in all mice groups showed no significant difference (Figure S11H). The heart size and weight in either the circ-ctrl–injected or mus_mecciNd2-injected mice were significantly increased upon TAC treatment, whereas mus_mecciNd2-injected mice demonstrated significantly less degree of increase (Figure 7G; Figure S11I). The increases in CM size and collagen accumulation during the transition from compensated cardiac hypertrophy to HF were described in the previous study.[42] In TAC mice, larger CM size and fibrosis area were observed in circ-ctrl–injected compared with the mus_mecciNd2-injected group (Figure 7H through 7J). The apoptosis marker caspase-3 was significantly lower in the mus_mecciNd2-injected group compared with the circ-ctrl–injected group (Figure 7H and 7K). These results are consistent with our speculation that mus_mecciNd2 administration in TAC mice extended the compensatory state and delayed the progression to HF.

Mus_mecciNd2 treatment blocked the increase in CypD as observed in the circ-ctrl group upon TAC surgery (Figure 7H and 7L). The decrease in TOMM20 levels was prevented, and the portion of TRAP1 overlapped with TOMM20 was kept at a normal level by

the administration of mus_mecciNd2 in TAC mice (Figure 7M; Figure S11J and S11K). These results demonstrated that mus_mecciNd2 application enhanced cardiac function and delayed the progression of TAC-induced HF.

DISCUSSION

Our results demonstrate the feature of fast degradation for mecciRNAs. The animal-conserved SUPV3L1/ELAC2 complex mediates mecciRNA degradation. In conditions associated with or triggering HF, SUPV3L1/ELAC2 levels and mecciRNA degradation are elevated in both cultured cells and the mouse heart. SUPV3L1/ELAC2 and mecciRNAs interact with mPTP and its regulators including TRAP1. The application of exogenous mus_mecciNd2, which interacts with cytosolic TRAP1, prevents the reduction of mitochondrial TRAP1 levels and mitigates deleterious mtROS release when cells and the heart are subjected to HF-inducing challenges (Figure 8). Administration of mus_mecciNd2 protects the heart in 2 mouse models of HF.

The interaction of SUPV3L1/ELAC2 with mitochondrial membrane complexes indicates that mecciRNA degradation may occur in proximity to these complexes. Therefore, a coupling between the levels of mecciRNAs and the activity of the complexes such as mPTP may be more achievable through close localization and interaction. SUPV3L1 and the exoribonuclease PNPase are core components of mitochondrial RNA degradosome, which is responsible for the degradation of linear RNAs in mitochondria.[19,20] It appears mitochondria-encoded mRNAs are degraded at a similar rate to mecciRNAs (Figure S1J and S1K). SUPV3L1 may be a key component for the degradation of both mecciRNAs and linear RNAs, and presumably a SUPV3L1-mediated regulatory orchestration may be present to manage different classes of mitochondrial RNAs. Currently, not much is known about the biogenesis of mecciRNAs.[9,13] The possibility that mecciRNAs may even be some degradation intermediates of mitochondrial linear RNAs cannot be excluded, although our data demonstrate that reasonable levels of mecciRNAs, and also maybe a set of special mecciRNAs including mecciND2, are necessary for the proper functionality of mitochondria.

TRAP1 as an HSP90 chaperone has regulatory roles, whereas ATP5B is both the catalytic subunit of the F1 complex and involved in mPTP regulation.[14,23–25] In that

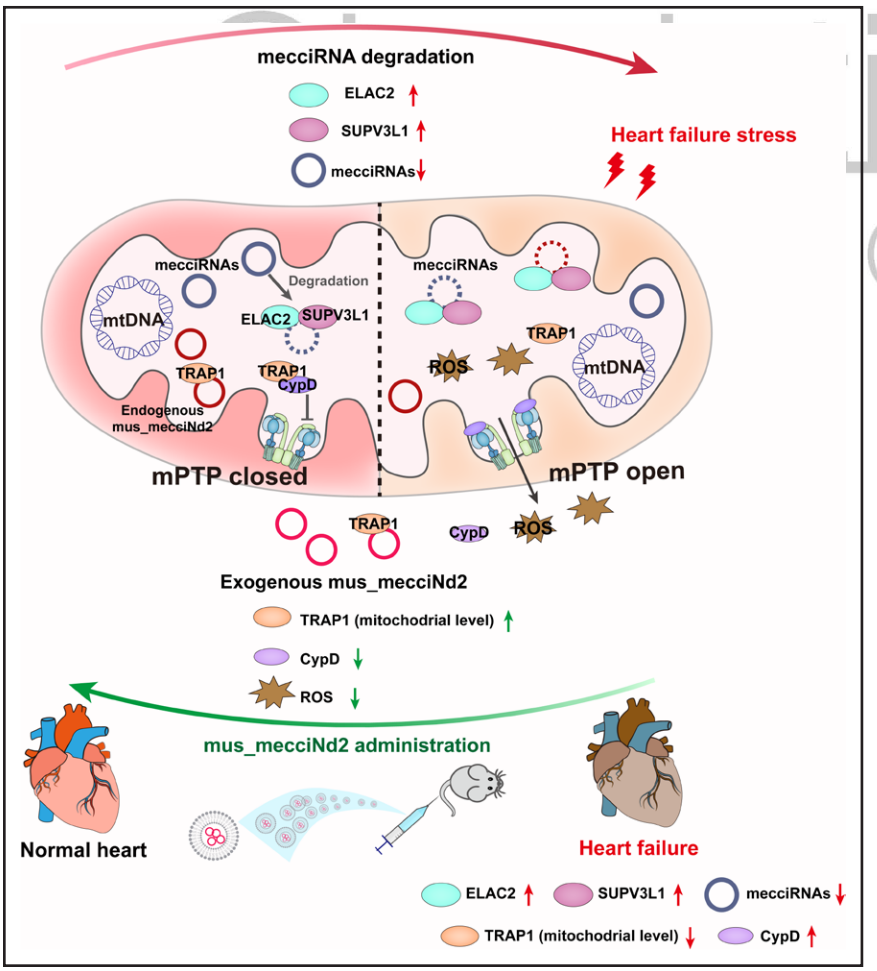

Figure 8. Working model of mecciRNA degradation and application of exogenous mecciND2 in tackling HF.
MecciRNAs are fast degraded in mitochondria by SUPV3L1 and ELAC2 complex. Under normal conditions, mecciRNAs bind to TRAP1 and facilitate the closing of the mitochondrial permeability transition pore (mPTP). In heart failure (HF) or HF-related stress conditions, the levels of SUPV3L1/ELAC2 and the degradation of mecciRNAs (including mecciNd2) are elevated in both cultured cells and the heart. Application of in vitro synthesized mus_mecciNd2 in cultured cardiomyocytes under HF conditions, such as doxorubicin and hypoxia, increases mitochondrial levels of TRAP1, decreases levels of CypD (a protein promoting mPTP opening), and ultimately prevents the opening of mPTP and the release of mitochondrial ROS. By modulating levels of TRAP1 and CypD, administration of exogenous mus_mecciNd2 exerts a protective effect on the mouse heart underlying HF-causing insults.

regard, targeting TRAP1 rather than ATP5B with mecciRNAs may be more adaptive in biomedical applications. Both SUPV3L1 and ELAC2 are multifunctional; however, SUPV3L1 heterozygous cells exhibit significantly higher levels of deleterious ROS, despite also having elevated mitochondrial mecciRNA levels to close the mPTP (Figure 4H through 4L). Therefore, directly targeting the mecciRNA degradation machinery may not be suitable; the application of exogenous mecciRNAs such as mecciND2 is sufficient to modulate mitochondrial levels of TRAP1 and CypD and thus may be more practical to be developed into therapeutics. Not having to be deliberately delivered into mitochondria for the exogenous mecciND2 to modulate the mitochondrial levels of TRAP1 would offer an advantage in developing mecciRNA therapeutics.

Prolonged mPTP opening promotes ROS production through ROS-induced ROS release, which is a positive feedback cycle triggered by the trafficking of released ROS between mitochondria that then stimulates the ROS generation of the surrounding mitochondria.[43] ROS-induced ROS release eventually leads to the elevation of the production of ROS throughout the cell. Application of mus_mecciNd2 antagonizes the vicious effects of DOX, hypoxia, or TAC procedure by reducing mPTP opening and inhibiting ROS output, and may eventually block ROS-induced ROS release in cultured cells or mouse hearts. In this study, we focused on the protective effects of mus_mecciNd2 through regulating mPTP and mROS release, which are mitochondria-based, and hopefully are applicable to both sexes. However, we acknowledge the importance of considering sex as a biological variable, because sex differences may affect the mechanisms and progression of HF.[1–4] Future studies are demanded to investigate the effects of mus_mecciNd2 in both sexes, and to realize the therapeutic potential of mecciND2.

HF remains incurable, and current treatment strategies focus on relieving symptoms and slowing the process to reduce mortality.[44] Several new drugs aiming to improve microcirculation, to prevent inflammation, or to protect myocardial interstitium are under development, and new drugs with novel strategies are still required to target dysfunctional cardiomyocytes and to recover their intrinsic function.[44,45] No specific anti-ROS therapy has been successfully developed to treat HF. Global antioxidants, such as vitamin C, vitamin E, and N-acetylcysteine, are reported to be beneficial to heart diseases based on small-scale investigations.[5] Several mitochondria-targeted antioxidant small molecules and peptides to scavenge mtROS under test have shown promising effects in HF treatment.[5] Here, starting from the discovery of fast degradation of mecciRNAs by the conserved SUPV3L1/ELAC2 complex, and the associated regulations of mecciRNAs on mPTP, we provide lines of evidence supporting the potential of harnessing the mecciRNA degradation mechanism and the exogenous mecciND2, which interacts with TRAP1, in effectively reducing the deleterious release of mtROS by maintaining the close state of mPTP to treat HF.

ARTICLE INFORMATION

Received June 5, 2024; accepted January 17, 2025.

Affiliations

Department of Cardiology, Department of Laboratory Medicine, First Affiliated Hospital of USTC, RNA Institute, School of Basic Medical Sciences, Division of Life Science and Medicine (X. Liu, Q.W., X. Li, Y.Y., Y.D., X.W., L.C., L.M., G.S.), Center for Advanced Interdisciplinary Science and Biomedicine of IHM (G.S.), University of Science and Technology of China, Hefei. Department of Ultrasound, First Affiliated Hospital of Anhui Medical University, Hefei, China (P.W.).

Acknowledgments

G.S. conceived of and designed this project. G. S., C.L., and L.M. supervised the experiments. X. Liu and Q.W. performed the experiments. X. Li, X. Liu, and P.W. built the mice model and performed echocardiography. Y.Y. built the pipeline for mecciRNA identification. X. Liu, Q.W., X.W., and Y.D. analyzed the RNA sequencing and experimental data. G.S., X. Liu, and Q.W. wrote the article. All authors have discussed the results and made comments on the article. All authors approved the final article. The authors thank Drs Haiming Wei (USTC) and Yajun Duan (USTC) for help and assistance in echocardiography experimental facilities and Dr Huafeng Zhang (USTC) for providing the hypoxia workstation. The authors also thank the Bioinformatics Center of the USTC, School of Life Sciences, for providing supercomputing resources and the Laboratory Animal Research Center of USTC for technical support.

Sources of Funding

This study was funded by the National Key R&D Program of China (2019YFA0802600), the National Natural Science Foundation of China (31930019, U23A20164, 32000438, 32200431, and 32270590), Research Funds of the Center for Advanced Interdisciplinary Science and Biomedicine of IHM (QYZD20230012), and Anhui Natural Science Foundation (2408085MC069).

Disclosures

G.S. and X.L. have an ownership interest in a patent related to this research.

Supplemental Material

Methods
Figures S1–S11
Supplemental Data S1–S6
Uncropped Gel Blots
References 46–50

REFERENCES

1. Bozkurt B, Coats AJ, Tsutsui H, Abdelhamid M, Adamopoulos S, Albert N, Anker SD, Atherton J, Bohm M, Butler J, et al. Universal definition and classification of heart failure: a report of the Heart Failure Society of America, Heart Failure Association of the European Society of Cardiology, Japanese Heart Failure Society and Writing Committee of the Universal Definition of Heart Failure. *J Card Fail*. 2021;27:387–413. doi: 10.1016/j.cardfail.2021.01.022
2. Schultheiss HP, Fairweather D, Caforio ALP, Escher F, Hershberger RE, Lipshultz SE, Liu PP, Matsumori A, Mazzanti A, McMurray J, et al. Dilated cardiomyopathy. *Nat Rev Dis Primers*. 2019;5:32. doi: 10.1038/s41572-019-0084-1
3. Seferovic PM, Polovina M, Bauersachs J, Arad M, Ben Gal T, Lund LH, Felix SB, Arbustini E, Caforio ALP, Farmakis D, et al. Heart failure in cardiomyopathies: a position paper from the Heart Failure Association of the European Society of Cardiology. *Eur J Heart Fail*. 2019;21:553–576. doi: 10.1002/ejhf.1461
4. Page RL 2nd, O'Bryant CL, Cheng D, Dow TJ, Ky B, Stein CM, Spencer AP, Trupp RJ, Lindenfeld J; American Heart Association Clinical Pharmacology and Heart Failure and Transplantation Committees of the Council on Clinical Cardiology; Council on Cardiovascular Surgery and Anesthesia; Council on Cardiovascular and Stroke Nursing; and Council on Quality of

Care and Outcomes Research. Drugs that may cause or exacerbate heart failure: a scientific statement from the American Heart Association. *Circulation*. 2016;134:32–69. doi: 10.1161/CIR.0000000000000426
5. Peoples JN, Saraf A, Ghazal N, Pham TT, Kwong JQ. Mitochondrial dysfunction and oxidative stress in heart disease. *Exp Mol Med*. 2019;51:1–13. doi: 10.1038/s12276-019-0355-7
6. Bauer TM, Murphy E. Role of mitochondrial calcium and the permeability transition pore in regulating cell death. *Circ Res*. 2020;126:280–293. doi: 10.1161/CIRCRESAHA.119.316306
7. Lopaschuk GD, Karwi QG, Tian R, Wende AR, Abel ED. Cardiac energy metabolism in heart failure. *Circ Res*. 2021;128:1487–1513. doi: 10.1161/CIRCRESAHA.121.318241
8. Chen L, Huang C, Shan G. Circular RNAs in physiology and non-immunological diseases. *Trends Biochem Sci*. 2022;47:250–264. doi: 10.1016/j.tibs.2021.11.004
9. Liu X, Wang X, Li J, Hu S, Deng Y, Yin H, Bao X, Zhang QC, Wang G, Wang B, et al. Identification of mecciRNAs and their roles in the mitochondrial entry of proteins. *Sci China Life Sci*. 2020;63:1429–1449. doi: 10.1007/s11427-020-1631-9
10. Kristensen LS, Andersen MS, Stagsted LVW, Ebbesen KK, Hansen TB, Kjems J. The biogenesis, biology and characterization of circular RNAs. *Nat Rev Genet*. 2019;20:675–691. doi: 10.1038/s41576-019-0158-7
11. Nielsen AF, Bindereif A, Bozzoni I, Hanan M, Hansen TB, Irimia M, Kadener S, Kristensen LS, Legnini I, Morlando M, et al. Best practice standards for circular RNA research. *Nat Methods*. 2022;19:1208–1220. doi: 10.1038/s41592-022-01487-2
12. Enuka Y, Lauriola M, Feldman ME, Sas-Chen A, Ulitsky I, Yarden Y. Circular RNAs are long-lived and display only minimal early alterations in response to a growth factor. *Nucleic Acids Res*. 2016;44:1370–1383. doi: 10.1093/nar/gkv1367
13. Ren B, Guan MX, Zhou T, Cai X, Shan G. Emerging functions of mitochondria-encoded noncoding RNAs. *Trends Genet*. 2023;39:125–139. doi: 10.1016/j.tig.2022.08.004
14. Zhao Q, Liu J, Deng H, Ma R, Liao JY, Liang H, Hu J, Li J, Guo Z, Cai J, et al. Targeting mitochondria-located circRNA SCAR alleviates NASH via reducing mROS output. *Cell*. 2020;183:76–93.e22. doi: 10.1016/j.cell.2020.08.009
15. Chen Z, He Q, Lu T, Wu J, Shi G, He L, Zong H, Liu B, Zhu P. mcPGK1-dependent mitochondrial import of PGK1 promotes metabolic reprogramming and self-renewal of liver TICs. *Nat Commun*. 2023;14:1121. doi: 10.1038/s41467-023-36651-5
16. Brzezniak LK, Bijata M, Szczesny RJ, Stepien PP. Involvement of human ELAC2 gene product in 3' end processing of mitochondrial tRNAs. *RNA Biol*. 2011;8:616–626. doi: 10.4161/rna.8.4.15393
17. Haack TB, Kopajtich R, Freisinger P, Wieland T, Rorbach J, Nicholls TJ, Baruffini E, Walther A, Danhauser K, Zimmermann FA, et al. ELAC2 mutations cause a mitochondrial RNA processing defect associated with hypertrophic cardiomyopathy. *Am J Hum Genet*. 2013;93:211–223. doi: 10.1016/j.ajhg.2013.06.006
18. Stepien PP, Margossian SP, Landsman D, Butow RA. The yeast nuclear gene suv3 affecting mitochondrial post-transcriptional processes encodes a putative ATP-dependent RNA helicase. *Proc Natl Acad Sci U S A*. 1992;89:6813–6817. doi: 10.1073/pnas.89.15.6813
19. Szczesny RJ, Borowski LS, Brzezniak LK, Dmochowska A, Gewartowski K, Bartnik E, Stepien PP. Human mitochondrial RNA turnover caught in flagranti: involvement of hSuv3p helicase in RNA surveillance. *Nucleic Acids Res*. 2010;38:279–298. doi: 10.1093/nar/gkp903
20. Borowski LS, Dziembowski A, Hejnowicz MS, Stepien PP, Szczesny RJ. Human mitochondrial RNA decay mediated by PNPase-hSuv3 complex takes place in distinct foci. *Nucleic Acids Res*. 2013;41:1223–1240. doi: 10.1093/nar/gks1130
21. Pearce SF, Rebelo-Guiomar P, D'Souza AR, Powell CA, Van Haute L, Minczuk M. Regulation of mammalian mitochondrial gene expression: recent advances. *Trends Biochem Sci*. 2017;42:625–639. doi: 10.1016/j.tibs.2017.02.003
22. Bogenhagen DF, Rousseau D, Burke S. The layered structure of human mitochondrial DNA nucleoids. *J Biol Chem*. 2008;283:3665–3675. doi: 10.1074/jbc.M708444200
23. Giorgio V, von Stockum S, Antoniel M, Fabbro A, Fogolari F, Forte M, Glick GD, Petronilli V, Zoratti M, Szabo I, et al. Dimers of mitochondrial ATP synthase form the permeability transition pore. *Proc Natl Acad Sci U S A*. 2013;110:5887–5892. doi: 10.1073/pnas.1217823110
24. Bonora M, Giorgi C, Pinton P. Molecular mechanisms and consequences of mitochondrial permeability transition. *Nat Rev Mol Cell Biol*. 2022;23:266–285. doi: 10.1038/s41580-021-00433-y
25. Kang BH, Plescia J, Dohi T, Rosa J, Doxsey SJ, Altieri DC. Regulation of tumor cell mitochondrial homeostasis by an organelle-specific Hsp90 chaperone network. *Cell*. 2007;131:257–270. doi: 10.1016/j.cell.2007.08.028
26. Cannino G, Urbani A, Gaspari M, Varano M, Negro A, Filippi A, Ciscato F, Masgras I, Gerle C, Tibaldi E, et al. The mitochondrial chaperone TRAP1 regulates F-ATP synthase channel formation. *Cell Death Differ*. 2022;29:2335–2346. doi: 10.1038/s41418-022-01020-0
27. Xiang F, Huang YS, Shi XH, Zhang Q. Mitochondrial chaperone tumour necrosis factor receptor-associated protein 1 protects cardiomyocytes from hypoxic injury by regulating mitochondrial permeability transition pore opening. *FEBS J*. 2010;277:1929–1938. doi: 10.1111/j.1742-4658.2010.07615.x
28. Giorgio V, Bisetto E, Soriano ME, Dabbeni-Sala F, Basso E, Petronilli V, Forte MA, Bernardi P, Lippe G. Cyclophilin D modulates mitochondrial F0F1-ATP synthase by interacting with the lateral stalk of the complex. *J Biol Chem*. 2009;284:33982–33988. doi: 10.1074/jbc.M109.020115
29. Lam SS, Martell JD, Kamer KJ, Deerinck TJ, Ellisman MH, Mootha VK, Ting AY. Directed evolution of APEX2 for electron microscopy and proximity labeling. *Nat Methods*. 2015;12:51–54. doi: 10.1038/nmeth.3179
30. Kaewsapsak P, Shechner DM, Mallard W, Rinn JL, Ting AY. Live-cell mapping of organelle-associated RNAs via proximity biotinylation combined with protein-RNA crosslinking. *eLife*. 2017;6:e29224. doi: 10.7554/eLife.29224
31. Cheng J, Nanayakkara G, Shao Y, Cueto R, Wang L, Yang WY, Tian Y, Wang H, Yang X. Mitochondrial proton leak plays a critical role in pathogenesis of cardiovascular diseases. *Adv Exp Med Biol*. 2017;982:359–370. doi: 10.1007/978-3-319-55330-6_20
32. Basit F, van Oppen LM, Schockel L, Bossenbroek HM, van Emst-de Vries SE, Hermeling JC, Grefte S, Kopitz C, Heroult M, Hgm Willems P, et al. Mitochondrial complex I inhibition triggers a mitophagy-dependent ROS increase leading to necroptosis and ferroptosis in melanoma cells. *Cell Death Dis*. 2017;8:e2716. doi: 10.1038/cddis.2017.133
33. Pinero J, Ramirez-Anguita JM, Sauch-Pitarch J, Ronzano F, Centeno E, Sanz F, Furlong LI. The DisGeNET knowledge platform for disease genomics: 2019 update. *Nucleic Acids Res*. 2020;48:D845–D855. doi: 10.1093/nar/gkz1021
34. Hua X, Wang YY, Jia P, Xiong Q, Hu Y, Chang Y, Lai S, Xu Y, Zhao Z, Song J. Multi-level transcriptome sequencing identifies COL1A1 as a candidate marker in human heart failure progression. *BMC Med*. 2020;18:2. doi: 10.1186/s12916-019-1469-4
35. Ye S, Chen W, Ou C, Chen MS. RNA sequencing reveals novel LncRNA/mRNAs co-expression network associated with puerarin-mediated inhibition of cardiac hypertrophy in mice. *PeerJ*. 2022;10:e13144. doi: 10.7717/peerj.13144
36. Riehle C, Bauersachs J. Small animal models of heart failure. *Cardiovasc Res*. 2019;115:1838–1849. doi: 10.1093/cvr/cvz161
37. Giordano FJ. Oxygen, oxidative stress, hypoxia, and heart failure. *J Clin Invest*. 2005;115:500–508. doi: 10.1172/JCI24408
38. Lu D, Chatterjee S, Xiao K, Riedel I, Huang CK, Costa A, Cushman S, Neufeldt D, Rode L, Schmidt A, et al. A circular RNA derived from the insulin receptor locus protects against doxorubicin-induced cardiotoxicity. *Eur Heart J*. 2022;43:4496–4511. doi: 10.1093/eurheartj/ehac337
39. Wallace KB, Sardao VA, Oliveira PJ. Mitochondrial determinants of doxorubicin-induced cardiomyopathy. *Circ Res*. 2020;126:926–941. doi: 10.1161/CIRCRESAHA.119.314681
40. Kehat I, Molkentin JD. Molecular pathways underlying cardiac remodeling during pathophysiological stimulation. *Circulation*. 2010;122:2727–2735. doi: 10.1161/CIRCULATIONAHA.110.942268
41. Ricci R, Eriksson U, Oudit GY, Eferl R, Akhmedov A, Sumara I, Sumara G, Kassiri Z, David JP, Bakiri L, et al. Distinct functions of junD in cardiac hypertrophy and heart failure. *Genes Dev*. 2005;19:208–213. doi: 10.1101/gad.327005
42. Furihata T, Kinugawa S, Takada S, Fukushima A, Takahashi M, Homma T, Masaki Y, Tsuda M, Matsumoto J, Mizushima W, et al. The experimental model of transition from compensated cardiac hypertrophy to failure created by transverse aortic constriction in mice. *Int J Cardiol Heart Vasc*. 2016;11:24–28. doi: 10.1016/j.ijcha.2016.03.007
43. Zorov DB, Juhaszova M, Sollott SJ. Mitochondrial reactive oxygen species (ROS) and ROS-induced ROS release. *Physiol Rev*. 2014;94:909–950. doi: 10.1152/physrev.00026.2013
44. Lam CSP, Docherty KF, Ho JE, McMurray JJV, Myhre PL, Omland T. Recent successes in heart failure treatment. *Nat Med*. 2023;29:2424–2437. doi: 10.1038/s41591-023-02567-2
45. Brown DA, Perry JB, Allen ME, Sabbah HN, Stauffer BL, Shaikh SR, Cleland JG, Colucci WS, Butler J, Voors AA, et al. Expert consensus document:

mitochondrial function as a therapeutic target in heart failure. *Nat Rev Cardiol*. 2017;14:238–250. doi: 10.1038/nrcardio.2016.203
46. Lian X, Hsiao C, Wilson G, Zhu K, Hazeltine LB, Azarin SM, Raval KK, Zhang J, Kamp TJ, Palecek SP. Robust cardiomyocyte differentiation from human pluripotent stem cells via temporal modulation of canonical Wnt signaling. *Proc Natl Acad Sci U S A*. 2012;109:1848–1857. doi: 10.1073/pnas.1200250109
47. Choi HMT, Schwarzkopf M, Fornace ME, Acharya A, Artavanis G, Stegmaier J, Cunha A, Pierce NA. Third-generation in situ hybridization chain reaction: multiplexed, quantitative, sensitive, versatile, robust. *Development*. 2018;145:dev165753. doi: 10.1242/dev.165753
48. Bao X, Guo X, Yin M, Tariq M, Lai Y, Kanwal S, Zhou J, Li N, Lv Y, Pulido-Quetglas C, et al. Capturing the interactome of newly transcribed RNA. *Nat Methods*. 2018;15:213–220. doi: 10.1038/nmeth.4595
49. Rausch JW, Heinz WF, Payea MJ, Sherpa C, Gorospe M, Le Grice SFJ. Characterizing and circumventing sequence restrictions for synthesis of circular RNA in vitro. *Nucleic Acids Res*. 2021;49:e35. doi: 10.1093/nar/gkaa1256
50. Shi L, Liu B, Shen DD, Yan P, Zhang Y, Tian Y, Hou L, Jiang G, Zhu Y, Liang Y, et al. A tumor-suppressive circular RNA mediates uncanonical integrin degradation by the proteasome in liver cancer. *Sci Adv*. 2021;7:eabe5043. doi: 10.1126/sciadv.abe5043